Nature Communications

https://doi.org/10.1038/s41467-026-69827-w

Article in Press

An interfacial-intramolecular electron highway for accelerated electrocatalytic CO_2 reduction by an O_2-tolerant formate dehydrogenase

Received: 13 August 2025

Accepted: 10 February 2026

Cite this article as: Liu, W., Zhang, P., Wang, X. *et al.* An interfacial-intramolecular electron highway for accelerated electrocatalytic CO_2 reduction by an O_2-tolerant formate dehydrogenase. *Nat Commun* (2026). https://doi.org/10.1038/s41467-026-69827-w

Weisong Liu, Peng Zhang, Xiufeng Wang, Kuncheng Zhang, Wenhua Yang, Huijuan Cui, Jun Liu, Junsong Sun, Chun You, Haiyang Cui, Zhiguang Zhu & Lingling Zhang

An interfacial-intramolecular electron highway for accelerated electrocatalytic CO_2 reduction by an O_2-tolerant formate dehydrogenase

Weisong Liu[1,2], Peng Zhang[3], Xiufeng Wang[4], Kuncheng Zhang[1,2], Wenhua Yang[5], Huijuan Cui[1], Jun Liu[1,2], Junsong Sun[2,6], Chun You[5], Haiyang Cui[4], Zhiguang Zhu[1,2], Lingling Zhang[1,2*]

[1] State Key Laboratory of Engineering Biology for Low-carbon Manufacturing, Tianjin Institute of Industrial Biotechnology, Chinese Academy of Sciences, Tianjin, 300308, China
[2] University of Chinese Academy of Sciences, Beijing 100049, China
[3] State Key Laboratory of Microbial Technology, Shandong University, Qingdao, 266237, China
[4] School of Life Sciences, Nanjing Normal University, Nanjing, 210046, China
[5] State Key Laboratory of Microbial Metabolism, School of Life Sciences and Biotechnology, Shanghai Jiao Tong University, Shanghai 200240, China
[6] Shanghai Advanced Research Institute, Chinese Academy of Sciences, Shanghai, 201210, China
[*]Corresponding author. E-mail address: zhangll@tib.cas.cn

Abstract

Bioelectrocatalytic CO_2 reduction offers a sustainable route for CO_2 bioconversion, yet remains limited by interfacial-intramolecular electron transfer and oxygen sensitivity. Here, we mine a formate dehydrogenase from *Shewanella oneidensis* MR-1 (*So*FdhAB) featuring completely oxygen tolerant and direct-electron-transfer (DET) electrocatalytic performances. Cryo-electron microscopy (Cryo-EM) analysis reveals an intramolecular electron highway comprising five [4Fe-4S] clusters, a regional face-face contact facilitating interfacial ET, and a unique oxygen resistance mechanism different from inactivation-activation. By acquiring a beneficial variant *So*FdhAB-Y94S, a direct bioelectrocatalytic CO_2 reduction system is constructed, accumulating 2.88 ± 0.03 mmol formate in 64 hours with a steady rate of 45.3 ± 0.5 μmol h^{-1} cm^{-2} and a Faradaic efficiency of 93.1 ± 5.2%. The merits of oxygen tolerance and efficient (electro)catalytic property endow *So*FdhAB a robust enzyme adopted in potential application scenarios, and the inherent DET capability may inspire the interfacial engineering of other oxidoreductases.

Introduction

The escalating global carbon dioxide (CO_2) emission has caused severe environmental and climate crisis, meanwhile, the rapid development in green biomanufacturing and synthetic biological technologies regards atmospheric CO_2 as a promising feedstock after sugar and biomass, considering its advantages of being nontoxic, abundant, and economic[1]. Despite the significant advancements in CO_2 biotransformation[2, 3], an essential issue rests with the activation of the inert CO_2 molecular. Large energy input as well as highly efficient catalysts are required. Electrochemical activation of CO_2 in mild conditions gains gradually attentions as the C1/C2 chemicals derived can be readily assimilated for further biosynthesis via microbial cell factories or multi-enzymatic systems[4-6]. Metal-based materials have emerged as the most effective electrocatalysts, while they suffer from the high overpotential leading to the considerable energy loss[7]. In contrast, bioelectrocatalytic CO_2 reduction via enzymes like formate dehydrogenase (FDH) lowers the activation energy largely, enabling the reaction occur close to the redox equilibrium potential[8-10]. For example, Hirst's group reported that the paradigm case of bioelectrocatalytic formate/CO_2 interconversion based on W-containing *Sf*FDH1 from *S. fumaroxidans*[10], and they also revealed that the mechanism of metal center valence changes in the interconversion of CO_2/formate through electrochemical methodologies[11-13]. Li et al reveal the direct electrochemistry of [4Fe-4S] cluster in *Cl*FDH from *Clostridium ljungdahlii*[14]. These studies confirm that metal-dependent FDHs function as thermodynamically reversible catalysts with low overpotential. Consequently, bioelectrocatalytic CO_2 reduction based on FDHs offers an attractive and economic approach in low-carbon green biotransformation.

Currently, bioelectrocatalytic CO_2 reduction faces the challenges of insufficient interfacial electron transfer (IET) at the enzyme-electrode interface, which severely constrains the potential application in biotransformation[15]. Direct electron transfer (DET) at the electrode interface, without any help of redox mediators is desired as it makes systems more energy-efficient, selective, stable, and scalable. Achieving complete DET is desired, however it remains difficult because most natural oxidoreductases are not intrinsically optimized for bioelectrocatalysis. In one hand, the active sites or ET spots of most natural oxidoreductases are often deeply buried in insulated protein shells, seriously hindering the DET. In the other hand, though, some enzymes such as hydrogenase[16, 17], carbon monoxide dehydrogenase[18-20], and complex I[21-23] containing iron-sulfur clusters as electron relay for direct electron transfer on electrodes, they may adopt random orientation when immobilized at the

electrode, sometimes making the DET pathway lengthy and convoluted[15, 20]. Electrode interface engineering and enzyme engineering have been applied to reinforce DET by promoting the oriented immobilization of enzymes and optimizing the IET pathway[24-26]. Lacey et al tried functionalized Au and graphite electrodes to induce the oriented immobilization of FdhAB from *Desulfovibrio vulgaris Hildenborough* (*Dv*H-FDH) via electrostatic interactions, and found the DET current is only 1/3 of the mediated electron-transfer (MET) current[27]. We truncated a hydrogen-dependent carbon dioxide reductase (HDCR) from *Thermoanaerobacter kivui* and employed its formate dehydrogenase counterpart (*Tk*FDH) for bioelectrocatalytic CO_2 reduction. Even though a certain amount of formate was produced, the poor IET efficiency (DET current/MET current) determines a quite sluggish electrocatalytic kinetics[28].

Another obstacle hindering the application of bioelectrocatalytic CO_2 reduction is the oxygen-induced deactivation of the anaerobic enzymes. There seems exists a trade-off effect between the enzymatic activity and oxygen tolerance. The HDCR from *Thermoanaerobacter kivui*[29, 30] and *Acetobacterium woodii*[31], and FDHs from *Syntrophobacter fumaroxidans*[32] exhibit fast catalytic kinetics with k_{cat} of 30-2650 s^{-1}, but they are anerobic enzymes. Oxygen tolerant FDHs, such as molybdenum (Mo)-containing FDHs from *Rhodobacter capsulatus*[33], *Cupriavidus necator*[34], and *Rhodobacter aestuarii*[35], and tungsten (W)-containing FDH from *Clostridium carboxidivorans*[36] and *Methylobacterium extorquens* AM1[37-40], as well as metal-independent FDHs[41], catalyze CO_2 reduction with the k_{cat} values below 1 s^{-1}. There are also exceptions. *Dv*H-FDH[42] and FDH from *Clostridium ljungdahlii* (*Cl*FDH) [14, 43] are DTT-activated anaerobic enzymes, and the activation mechanism of *Dv*H-FDH was recently illustrated as the reduction of disulfide linkage and the switch-on of the substrate entry channel[44], but the oxygen-attacking mechanism of more FDHs is unclear. Thus, to seek a FDH of high IET efficiency and oxygen-tolerance at the same time is challenging yet promising in application.

Here, we identify an oxygen-tolerant W-containing formate dehydrogenase from *Shewanella oneidensis* MR-1 (*So*FdhAB) with high catalytic and electrocatalytic efficiency, through AI-assisted enzyme mining using *Tk*FdhF as the starting template. Kinetic study demonstrates its higher activity than *Tk*FdhF and the natural oxygen-tolerant feature. *So*FdhAB can achieve firm orientation on electrodes, enabling electrocatalytic CO_2 reduction with approaching 100% IET efficiency. By analyzing the influencing factors obtained from a combination of three approaches, electrode interface engineering, enzyme engineering, and Cryo-EM, it is concluded that the efficient IET

efficiency of *So*FdhAB is, as expected, attributable to two factors, 1) the canonical intramolecular electron highway composed of the [4Fe-4S] clusters, 2) The distal [4Fe-4S] cluster and the surrounding aromatic residues at the proximity of the surface of subunit FdhB. Additionally, the oxygen-protection mechanism of *So*FdhAB, without any reductive activation, is revealed. Finally, a beneficial variant *So*FdhAB-Y94S with improved catalytic current is employed to build a bioelectrocatalytic system for formate production from CO_2. This work provides a promising candidate for the potential application of bioconversion of CO_2, and the unique structure of *So*FdhAB that is conducive to efficient IET efficiency establishes a valuable insight for interfacial engineering of other oxidoreductases to achieve desired efficient IET in bioelectrocatalysis.

Results and Discussion

Mining of high-active and oxygen-tolerant formate dehydrogenase

HDCR from *Thermoanaerobacter kivui* was reported as the most efficient CO_2 reductase[29, 30], and its FDH counterpart was demonstrated to be electro-responsive[28]. Taking its amino acid sequence as the template of AI-assisted enzyme mining, 32,223 potential sequences was retrieved in total via applying rigorous criteria (30% to 50% sequence identity and 80% bidirectional sequence coverage) in a large-scale homology search against a dataset of 250 million protein sequences in the UniProt database (TrEMBL) using Diamond tool. Subsequently, CLEAN tool[45] was employed to annotate their functions with a confidence threshold of 0.5, narrowing the dataset to 5,728 sequences. Further classification by EC numbers and redundancy elimination excludes subsets such as metal-independent FDHs sequences as EC 1.17.1.9, and 2,256 potential metal-dependent FDHs sequences were pinpointed. Among them, 968 sequences were predicted by CataPro tool[46] to be more efficient than *Tk*FDH. To ensure oxygen tolerance, 135 sequences from anaerobic bacteria were excluded, leaving 833 sequences from aerobic or facultative anaerobic (Supplementary data 1, Fig. 1a). A phylogenetic analysis undergoes on these 833 sequences using IQ-Tree (Supplementary data 2, Fig. 1b) and the evolutionary tree is divided into three main branches, including FDH-N branch, FDHs alpha on the same evolutionary branch with *Tk*FdhF, and distantly related FDH branch. Notably, as high as 63 sequences sourced from *Shewanella* species. Since *Shewanella oneidensis* MR-1 had been shown to perform microbial electrocatalytic CO_2 reduction to produce formate, and the rate can be increased when its fdhA1 and fdhB1genes were strengthened[47], FdhA1B1C1 from *Shewanella oneidensis* MR-1 was concentrated.

The encoded peptides in the gene cluster *fdhA1B1C1* include chaperone FdhT (So_4507), accessory protein FdhX (So_4508), formate dehydrogenase molybdopterin-binding subunit, FdhA (So_4509), formate dehydrogenase FeS subunit FdhB (So_4510), and formate dehydrogenase cytochrome b subunit FdhC (So_4511) (Supplementary Fig. 1a). FdhT likely aids folding and assembly of metal active center of FdhA. FdhX may bind to the twin-arginine translocation signal peptide to facilitate protein transport and further active maturation of FdhA. FdhA1B1C1 could be a heterotrimer composed by formate dehydrogenase molybdopterin-binding subunit, formate dehydrogenase FeS subunit and formate dehydrogenase cytochrome b subunit (Supplementary Fig. 1a and 1b). Considering the functional subunits of interests and avoiding the complicate purification of membrane-bound protein, the membrane-binding subunit FdhC was truncated and generated the active *So*FdhAB in *Shewanella oneidensis* MR-1Δ*fdhAB* (Supplementary Fig. 1c and Supplementary Fig. 2). Additionally, *So*FdhA was also constructed and expressed as a control (Supplementary Fig. 1d). Two bands of approximately 99 kDa and 23 kDa, corresponding to *So*FdhA and *So*FdhB respectively, were observed in the SDS-PAGE image (Fig. 1c). As a newly-found enzyme, the W, Mo and iron atoms contents in *So*FdhAB were determined by ICP-MS (Supplementary Table 1). A W content of 0.78 ± 0.10 mol per mol of protein was detected, while only 0.05 ± 0.02 mol of Mo was present. These results suggested that *So*FdhAB is a W-dependent enzyme, rather than the labeled Mo-dependence in gene annotation. In addition, although only 14.91 ± 3.64 mol of iron was detected, the iron-to-tungsten ratio was 18.84 ± 2.23, implying probably five [4Fe-4S] clusters exist in *So*FdhAB.

The CO_2 reduction activity of *So*FdhAB was assayed as high as 52.5 ± 1.9 s^{-1} (Fig. 1d), which is approximately 5-times higher than that of *Tk*FdhF, although the formate oxidation activity reached 253.1 ± 5.8 s^{-1} (Fig. 1e). As controls, *So*FdhA showed slight catalytic activity towards both CO_2 reduction and formate oxidation, and the activity of metal-free *So*FdhAB* was lost (Fig. 1d and 1e), suggested that the W ions and FdhB subunit are essential for the integrity of *So*FdhAB. The role of FdhB subunit was similar to that of HycB3 in *Tk*FdhF_HycB3 as an electron transfer subunit[28, 30]. It was worth mentioning that *So*FdhAB exhibits an excellent oxygen tolerance throughout the entire process of expression, purification, operation, and storage, outperforming other high-active anaerobic Mo/W-containing formate dehydrogenases[13, 48, 49] and facilitating the potential application.

Bioelectrocatalytic characterization of *So*FdhAB

*So*FdhAB/carbon nanotube/glassy carbon electrode (*So*FdhAB/CNT/GC) electrode was constructed to study the basic electrocatalytic behaviors of *So*FdhAB. The voltammograms recorded

at different pH value demonstrate that *So*FdhAB catalyzed the reversible interconversion of CO_2 and formate, and acidic electrolyte was beneficial for CO_2 reduction (Supplementary Fig. 3) by inhibiting the hydration of CO_2[50]. The current density for formate oxidation was 4-times higher than that of CO_2 reduction at pH 7.0, aligning well with the catalytic trend in solution. In addition, the onset potential for CO_2 reduction was -420 mV *vs.* SHE at pH 7.0 (Supplementary Fig. 3c), close to the formal formic acid/CO_2 redox potential (−412 mV *vs.* SHE at pH 7.0) [10, 51]. The catalytic current for both CO_2 reduction and formate oxidation decreased at pH 5.0 (Supplementary Fig. 3a), resulting from *So*FdhAB deactivation (Supplementary Fig. 4).

A rotating disk electrode (RDE) was employed to study the electrocatalytic kinetics and the LSVs of *So*FdhAB/CNT/RDE at different rotations rates (0, 25, 64, 100, 400, 900 rpm) were recorded (Fig. 2a). The stationary catalytic current density was 1.8 mA cm^{-2}, limited by mass transfer. When the rotation speed raised to 25 rpm or higher, the current density increased more than twofold and kept nearly constant, demonstrating a kinetic-limiting process. This phenomenon was different from that of FdhF_HycB3Δ159-184, which generated the constant current with the increase of rotation speeds from 0-900 rpm and demonstrated an absolute enzymatic kinetics-controlled process[28]. To study the mechanism behind, the kinetics parameters for CO_2 reduction and formate oxidation were determined (Supplementary Fig. 5). As shown in Supplementary Fig. 5c, the current density reached maximum 5.4 ± 0.4 mA cm^{-1} when the concentration of CO_2 was higher than 25 mM. The function between current density and substrate concentration was consistent with the Michaelis-Menten equation, indicating that enzyme kinetics is the main factor limiting electrode performance. The apparent K_M value was calculated as 4.8 ± 0.4 mM, higher than that of other W-containing FDHs[28, 42], indicating a lower affinity for CO_2, which may be the cause of mass transfer limitation for the stationary electrode. In addition, the concentration of 25 mM corresponding to the maximum current was lower than the saturated CO_2 concentration (~33 mM at standard pressure and room temperature), interpreting the elimination of mass transfer limitation upon the rotation. In comparison, the apparent K_M value of formate was calculated as 9.7 ± 0.8 mM (Supplementary Fig. 5d), which was higher than that of CO_2 and demonstrated the catalytic preference of *So*FdhAB towards formate oxidation may be attributed to its higher catalytic efficiency, rather than its affinity to formate.

DET-type bioelectrocatalysis are always pursued, especially the remarkable IET efficiency. By investigating the DET-type and MET-type bioelectrocatalytic CO_2 reduction at *So*FdhAB/CNT/GC electrodes (Fig. 2c), it is surprisingly found that the DET-type current density for CO_2 reduction

reached as high as 4.1 ± 0.3 mA cm^{-2} at –550 mV vs. SHE, and the IET efficiency achieved > 0.9 (Fig. 2d and 2e, Supplementary Fig. 6), indicating that *So*FdhAB undergoes a smooth electron communication with the electrode and it may naturally adopts a favorable orientation for efficient DET. To explore the possible driving forces for the favorable orientation of *So*FdhAB, different functionalized CNT electrodes were employed. The catalytic currents via DET and MET modes of *So*FdhAB on CNT, amino-modified carbon nanotubes (NH_2-CNT), carboxyl-modified carbon nanotubes (COOH-CNT), graphitized carbon nanotubes (gCNT), and the carbon nanotubes doped with pyrene methylamine (PMA-CNT) were recorded and compared (Fig. 2b). As show in Fig. 2d, the current density on NH_2-CNT electrode was higher than that on CNT electrode, while equivalent to that on COOH-CNT electrode. These results suggested that *So*FdhAB may form hydrogen bond interactions rather than electrostatic attraction to adsorb onto the electrode surface. This phenomenon was further verified by that the current density on more hydrophobic gCNT was significantly decreased. The current density on PMA-CNT electrode was further increased compared to that on NH_2-CNT, which indicated that the π-π interaction might also form between *So*FdhAB and pyrene ring of electrode surface for immobilizing enzyme. It was worth noting that the ratio of DET/MET current kept always higher than 0.9 at most of the electrodes except for gCNT electrode (Fig. 2e), suggesting that the driving force for the oriented immobilization of *So*FdhAB is a synergistic effect of hydrogen bond interaction and π-π stacking, which was hard to alter along with the changes of surface properties.

Cryo-EM structure guided molecular mechanism understanding on electrocatalysis

In order to further study the (electro)catalytic mechanism of *So*FdhAB, the structural information is necessary and thereby Cryo-EM was employed to acquire its structure (Supplementary Fig. 7). Through 2D classification and 3D model reconstruction, a final map was obtained with an overall resolution of 2.75 Å, as determined by gold-standard Fourier shell correlation (FSC) at the 0.143 criterion. The entire spatial structure of *So*FdhAB was composed of catalytic subunit FdhA and the electron-transfer subunit FdhB (Fig. 3b). FdhA subunit contained one W-binding bis-pterin guanine dinucleotide (W-bis-PGD) cofactor and one [4Fe-4S] cluster, and FdhB subunit binds four [4Fe-4S] clusters for electron transfer (Fig. 3a), consistent with the measured 1:5 of W-center and [4Fe-4S] clusters by ICP-MS (Supplementary Table 1). Similar structure was also observed in *Dv*H-FDH[42], *Tk*FdhF[30] and *Ec*FDH-H[52] from *E. coli*. Moreover, it was evident from Fig. 3a that the FeS clusters were likely to form an electron relay, with inter-cluster distances under 10.6 ± 1.2 Å permitting

efficient electron tunneling to the active site. According to Marcus theory, the electron shuttling rate is a function of the potential difference, reorganization energy and the distance between the electrode matrices and ET spots of oxidoreductases. Basically, electrons can theoretically shuffle in a fast rate within 14 Å between redox centres[53] and the 20 Å was estimated to be the maximum distance for interfacial, intermolecular, or intramolecular electron tunneling[54, 55]. Five pairs of salt bridges (R844-D45, R260-E50, E246-R12, R110-D28 and E90-K149) at the interface of FdhA and FdhB acted as molecular zipper to stabilize two subunits (Fig. 3c, Supplementary Fig. 8). Interestingly, the basic and acidic amino acids that formed these five salt bridge pairs were arranged alternately, which may help stabilize the proper conformation between FdhA and FdhB and ensure the fixed distance between A1 and B1 [4Fe-4S] clusters. Similar interactions existed widely in enzyme complexes like ferredoxin-$NADP^+$ reductases (FNRs) [56, 57].

Apart from the intramolecular electron highway, the IET had been studied. By analyzing the proximal residues of the distal B4 [4Fe-4S] cluster, it was deduced that three sites, Y94, Y97, and F112, may contribute to the interaction with the electrode surface (Fig. 3d). Site-directed mutagenesis was carried out by substituting with alanine (eliminating hydrogen bonds and π-π interactions), phenylalanine (eliminating hydrogen bonds but retaining π-π interactions), and serine (eliminating π-π interactions but retaining hydrogen bonds), respectively, at these three positions. As a result, four variants, Y97A, Y97F, Y94F and Y94S, folded properly and remained the catalytic functions (Fig. 3e). They showed the varied catalytic activity towards CO_2 reduction, suggesting the predominated role of B4 cluster in catalysis. Afterwards, the electrocatalytic performances of four variants were evaluated at pristine CNT electrodes, NH_2-CNT modified electrodes and PMA-CNT modified electrodes. As displayed in Fig. 3f, the catalytic current of *So*FdhAB-Y94S was 1.5-fold higher than that of wild type on CNT, NH_2-CNT and PMA-CNT electrodes. The average coverage (Γ) of enzyme molecules, determined from the non-turnover redox peaks, was comparable for *So*FdhAB ($3.6 \pm 0.001 \times 10^{-10}$ mol cm^{-2}) and *So*FdhAB-Y94S ($3.9 \pm 0.002 \times 10^{-10}$ mol cm^{-2}) (Supplementary Fig. 9). These results suggested that the enhanced catalytic current was not attributed to enzyme loading. In another aspect, no obvious solution activity increase was observed (Fig. 3e), suggesting that the increase in catalytic current cannot be attributed to catalytic activity either. We further analyzed the structure and performed molecular dynamics (MD) simulation. Compared with tyrosine, the side chains of serine were shortened by 4.8 Å and the loop at the bottom has deflected upward by 53.4° in *So*FdhAB-Y94S (Supplementary Fig. 10a), and the distances between distal Fe-S cluster and CNT surface of

*So*FdhAB-Y94S were shorter than that of *So*FdhAB (Supplementary Fig. 10b-10f). These results indicated that the possible reason of increased catalytic current might be that the serine substitution shortened the distance between distal Fe-S cluster and the electrode surface. Additionally, polar serine may help to break the hydration layer and form hydrogen bonds with the –OH, -COOH, -NH_2 groups of CNT electrodes[58], facilitating the firm immobilization of enzymes on electrodes. The significantly decreased current of Y94F, compared to variant *So*FdhAB-Y94S, confirms the hydrogen bond interaction, instead of π-π interactions. The tyrosine residue at position 97 possibly interacted with the electrode via π-π interactions, because substituting tyrosine with phenylalanine didn't change the current values too much, but substituting tyrosine with alanine significantly decreased the current at PMA-CNT electrodes. When IET efficiency was analyzed, it was found that all four variants maintain the value up to 0.9 (Fig. 3g), implying the oriented immobilization of *So*FdhAB was a regional synergistic effect of hydrogen bonds and π-π interactions, namely face-face contact, and a single-point mutation was difficult to significantly destroy its binding conformation on the electrode.

Further understanding on the molecular mechanism of interfacial electron highway were obtained by comparing and analyzing the distal [4Fe-4S] clusters in *So*FdhAB, FdhF_HycB3Δ159-184, and *Dv*H-FDH (Fig. 3h and 3i). *Dv*H-FDH contained only three [4Fe-4S] clusters in the small subunit, and the distal [4Fe-4S] cluster was located 17.1 Å away from the nearest surface, making the IET less sufficient than that of *So*FdhAB (Fig. 3h). Additionally, the bottom surface of the *Dv*H-FDH subunit was mainly occupied by acidic amino acids (D87, D89 and E91), and it favored the oriented immobilization at positively charged (e.g., $NHMe_2^+$) electrode. However, the single-type weak interaction may not afford high IET efficiency[26, 27]. In the case of FdhF_HycB3Δ159-184, its distal [4Fe-4S] cluster was close to the protein surface (3.3 Å), but the residues around it were mainly aliphatic uncharged amino acids (I84, T88, P65 and V63) (Fig. 3i), which hardly directed the highly-ordered enzyme orientation at the electrode[28]. *So*FdhAB contained not only a B4 [4Fe-4S] cluster closed to the protein surface (4.3 Å) for playing an electron relay between enzyme and electrode, but also key residues (Y97, Y94, and F112) surrounded (Fig. 3d) inducing the uniform binding via synergistic effects of hydrogen bond interactions and π–π stacking. To conclude it, the unique B4 cluster microenvironment endowed *So*FdhAB the nature of DET capability, making it a model for studying IET between enzymes and electrodes.

Cryo-EM structure guided molecular mechanism understanding on oxygen tolerance

*So*FdhAB exhibited remarkable oxygen insensitivity. Unlike the DTT-involved oxygen protection

of *Dv*H-FDH, interpreting as an allosteric redox switch of disulfide linkage between C845 and C872[44], the activity of *So*FdhAB kept unchanged before and after DTT treatment (Fig. 4a and 4b). To understanding the molecular basis of this distinct behavior, the sequence and structure of *So*FdhAB was aligned with *Dv*H-FDH. *So*FdhA and *So*FdhB shared 30.5% and 22.5% sequence identity with *Dv*H-FDHA and *Dv*H-FDHB, respectively. However, the metal active sites were relatively conserved (Supplementary Fig. 11a), apart from a selenocysteine substitution in *Dv*H-FDHA (Supplementary Fig. 11b and 11c). To further understanding the molecular mechanism on oxygen tolerance, we compared the structure of *So*FdhA subunit of *So*FdhAB with anaerobic FDH from *Acetobacterium woodii* (*Aw*FDH, modeled by AlphaFold 3)[31], anaerobic FDH from *E. coli* (*Ec*FDH, PDB:1FDI) [59], anaerobic FDH from *Thermoanaerobacter kivui* (*Tk*FDH, PDB: 7QV7) [30], and with oxygen-tolerant FDH from *Desulfovibrio vulgaris Hildenborough* (*Dv*H-FDH, PDB: 6SDR) [42]. As shown in Supplementary Fig. 12, both *So*FdhA and *Dv*H-FDH have extra two domains compared with other three anaerobic FDHs, suggesting that these domains may play key role in oxygen protection. A distinct difference was observed in domain 1, and the spatial positions corresponding to C845 and C872 in *Dv*H-FDH, which comprised D808 and T777 in *So*FdhAB. *So*FdhAB has different substrate channel from *Dv*H-FDH, and the exit of the gas substrate tunnel was controlled by H653 and V666 in domain 2 rather than cysteines (Fig. 4c), which further supporting the apparent observation that *So*FdhAB didn't require reductive activation. In addition, a bulky residue Y776 were blocked in the tunnel (Fig. 4c). To further reveal the role of this residue on oxygen tolerance, variant *So*FdhAB-Y776A was constructed, and found that the activity of *So*FdhAB-Y776A variant was reduced by 37% under aerobic expression and purification. Interestingly, under anaerobic, the activity of *So*FdhAB-Y776A has recovered to be basically equivalent to that of *So*FdhAB wild type (Fig. 4d and 4e). Further analysis on the structure difference between *So*FdhAB and *Dv*H-FDH identified that another residue T927 located on the opposite side of Y776 residue was also locked onto this channel (Fig. 4c). Thus, *So*FdhAB-Y776A/T927A variant was also constructed based on *So*FdhAB-Y776A variant, and activity assay found that *So*FdhAB-Y776A/T927A variant was affected even more dramatically under aerobic, while the activity of *So*FdhAB-Y776A/T927A has significantly increased under anaerobic (Fig. 4d and 4e). These results suggested that Y776 and T927 play a key role in oxygen protection.

Bioelectrocatalytic synthesis formate from CO_2

*So*FdhAB-Y94S variant was employed to construct bioelectrode because it exhibited higher catalytic current than *So*FdhAB-WT (Fig. 3f, Fig. 5a). The catalytic current of *So*FdhAB-Y94S under

PMA-CNT electrodes was slightly higher than that on NH_2-CNT electrodes. However, the stability of *So*FdhAB-Y94S under PMA-CNT electrodes was significantly lower than that on NH_2-CNT electrodes during the long-range reaction (Supplementary Fig. 13). Thus, a *So*FdhAB-Y94S/amino-modified carbon nanotubes/carbon paper (*So*FdhAB-Y94S/NH_2-CNT/CP, 1×1 cm^2) electrode was constructed (Fig. 5b). A catalytic current of -2.9 ± 0.4 mA cm^{-1} was observed upon the introduction of CO_2 gas at a potential of -600 mV *vs.* SHE, and i-t curve was recorded over 30-hour reaction period (Fig. 5b). After the initial 6 hours of reaction, the pH of the electrolyte decreased from 7.0 to 4.9, and such a low pH would lead to the enzyme deactivation (Supplementary Fig. 4,). When the electrolyte was refreshed and the electrode was cleaned, the catalytic current recovered. The concentration of formate product was monitored by HPLC. As shown in Fig. 5c, a formate of 878.6 ± 81.5 μmol was accumulated within 30 h with a Faradaic efficiency of 97.0 ± 1.5%. The average rate for producing formate was 29.3 ± 2.7 μmol h^{-1} cm^{-2}, which was 3-fold higher than that achieved by *Dv*H-FDH at same potential of −600 mV *vs.* SHE (10 μmol h^{-1} cm^{-2})[60], and more than tenfold higher than that of the bioelectrocatalytic system catalyzed by FdhF_HycB3Δ159–184 at −500 mV *vs.* SHE[28] (Table 1). The reaction rate in fourth reaction cycle remains 16.5 ± 1.2 μmol h^{-1} cm^{-2}, still higher than that catalyzed by *Dv*H-FDH at the same applied voltage. To avoid the reduction of system pH caused by the anodic electrolytic water reaction, we carried out the electrocatalytic reaction in the H-cell system. The system can operate stably for 64 hours (Fig. 5d), accumulating 2.88 ± 0.03 mmol formate, with a production rate of 45.3 ± 0.5 μmol h^{-1} cm^{-2}, and a Faradaic efficiency of 93.1 ± 5.2% (Fig. 5e). So far, it represents the best-performing candidate for bioelectrocatalytic CO_2 reduction systems considering both the production rate and the energy efficiency (Table 1).

To evaluate the potential application of the as-constructed bioelectrocatalytic CO_2 reduction system, gas mixture with low concentrate CO_2 (10% CO_2+20% O_2+70% N_2) and the simulated syngas (40% CO_2+40% CO+20% H_2) was employed. As shown in Fig. 5d, a current density of 1.6 mA cm^{-2} was produced and no obvious current decrease was observed in 6 hours, validating the excellent oxygen tolerance of *So*FdhAB-Y94S. A rate of 46.4 ± 4.3 μmol h^{-1} cm^{-2} was achieved in this system despite the decreased Faradaic efficiency caused by oxygen reduction (Fig. 5h). In the case of syngas, a current density of 3.0 mA cm^{-2} was generated (Supplementary Fig. 14a and 14b) and the formate production rate was 23.6 ± 4.2 μmol h^{-1} cm^{-2} without coulombic loss (Faradic efficiency of 99.2%) (Supplementary Fig. 14c). These results indicate that *So*FdhAB-Y94S has the ability to reduce the CO_2 in both anaerobic and aerobic gases, and was applied to a wide range of potential application

scenarios.

In summary, we identified *So*FdhAB as a highly active and oxygen-tolerant formate dehydrogenase that exhibited >90% IET efficiency on electrodes. This represents a significant result in bioelectrocatalysis, where such high IET efficiency is uncommon among natural oxidoreductases. Cryo-EM revealed that *So*FdhAB contained an intramolecular electron highway composed of five iron-sulfur clusters, providing the structural basis for its high (electro)catalytic activity. Additionally, the unique microenvironment of the distal Fe–S cluster, located close to the protein surface and surrounded by aromatic amino acids, played a key role in oriented immobilization through hydrogen bonds and π–π stacking interactions with the electrode surface, thereby enabling remarkable IET efficiency. An enlarged bioelectrode based on *So*FdhAB-Y94S with enhanced catalytic current was constructed for the electrosynthesis formate from CO_2, producing 878.6 ± 81.5 μmol formate in 30 hours, with a production rate of 29.3 ± 2.7 μmol h^{-1} cm^{-2} and a Faradaic efficiency of 97.0 ± 1.5%. In H-cell system, stable operation time has been increased to 64 hours, and the accumulation of formate was enhanced to 2.88 ± 0.03 mmol and the production rate was improved to 45.3 ± 0.5 μmol h^{-1} cm^{-2}. *So*FdhAB-Y94S also exhibited efficient applicability under the simulated industrial scenario. Our work provided an oxygen-tolerant and highly active FDH, establishing a paradigm case for electrocatalytic CO_2 reduction with efficient IET. This advances an important step toward the application of formate dehydrogenase in industrial-scale synthesis formate from CO_2.

Methods

Reagents and materials

All the chemicals of analytical grade or higher purity were purchased from Sinopharm (Beijing, China) Merck, Macklin (Shanghai, China) unless otherwise noted. Carbon nanotubes (CNTs), amino modified carbon nanotubes (NH_2-CNT), carboxyl-modified carbon nanotubes (COOH-CNT) and graphitized carbon nanotubes (gCNT) with a diameter of 5-15 nm were purchased from XFNANO (Nanjing, China), and carbon papers were obtained from TORAY, Japan. The PrimeSTAR Max DNA Polymerase was obtained from Takara Bio (Japan). A ClonExpress-II one-step cloning kit was purchased from Vazyme (Nanjing, China). The methylation sensitive restriction enzyme (*Dpn*I) was obtained from New England Biolabs. All primers and genes were synthesized and sequencing service was provided by Tsingke (Beijing, China). Lysogeny Broth (LB) medium (1 L) containing 10 g of NaCl, 10 g of tryptone and 5 g of yeast extract. For the LB agar plates, 20 g of agar was added. All the media were then autoclaved at 121°C for 20 min.

AI-assisted enzyme mining

The protein sequence of *Tk*FdhF from was used as template for blast in the UniProt database (TrEMBL). Diamond tool was used for a large-scale homology search, and sequence identity of 30%-50% and bidirectional sequence coverage of 80% was applied. A total of 32,223 potential sequences were retrieved. Following, their functions was annotated by CLEAN tool with a confidence threshold of 0.5. 5,728 sequences with reliable functional annotations were further classified by EC numbers, and the metal-independent FDHs, some nitrate reductase sequence and redundant sequences were excluded to narrow dataset to 2256. The enzyme kinetic constants (k_{cat}/K_M) of these metal-dependent FDHs were predicted utilized the CataPro tool. A total of 968 sequences with higher $k$cat/K_M than the starting template were selected. Among them, 135 sequences from anaerobic bacteria were removed. The phylogenetic analysis of the rest of 833 metal-dependent FDH sequences were performed via IQ-Tree using the Maximum Likelihood (ML) approach[61]. The best-fit amino acid substitution model was identified as LG+I+R10 by ModelFinder based on the Bayesian Information Criterion (BIC). Reliability of the internal branches was assessed using 1,000 ultrafast bootstrap replicates (UFBoot). The tree was analyzed and visualized by Interactive Tree of Life (iTOL), and the phylogenetic tree was rooted using the *Tk*FdhF sequence as a reference template, distinct branches were annotated with taxonomic information and predicted catalytic properties to facilitate the identification of diverse clusters[62].

Knocking-out of gene *fdhAB* in *Shewanella oneidensis* MR-1

The suicide plasmid pHG1.0 and 2,6-diaminopimelic acid (DAP) dependent strain *E. coli* WM3064 Δ*dapA* (Host for pir-dependent plasmids and donor strain for conjugation) were gifts from Prof. Liu. Homologous recombination-mediated gene knockout was used to delete fdhA and fdhB in the genome of *Shewanella oneidensis* MR-1[63]. Homologous arms fragments (500 bp each) located upstream of *fdh*A and downstream of *fdh*B were ligated and inserted into suicide plasmid pHG1.0 to construct the knockout plasmid. The knockout plasmid was transformed into *E. coli* WM3064 Δ*dapA*, and the single clone was selected from the LB agar plates with 50 mg L^{-1} ampicillin and 50 mg L^{-1} DAP. The donor strain *E. coli* WM3064 Δ*dapA* was cultured at 37°C in LB medium supplemented with 50 mg L^{-1} ampicillin and 50 mg L^{-1} DAP until an OD_{600} of 0.4–0.6, while the recipient strain *Shewanella oneidensis* MR-1 was cultured at 30 °C in LB medium until an OD_{600} of 0.4–0.6. 2 ml of donor cells and 1 ml recipient cells by centrifugation at 3000 x g for 1 minutes respectively. The *E. coli* WM3064 Δ*dapA* cells were washed with fresh LB once, and donor cells and recipient cells were resuspended

and mixed by 200 μL LB with 50 mg L^{-1} DAP. The mixture was incubated for 6 hours at 30 °C for conjugative transfer, followed by centrifugation at 3000 x g for 1 minute. The cells were resuspended and washed twice with 1 mL of fresh LB, then applied onto LB agar plates containing 15 mg L^{-1} gentamicin for cultivating 24 h at 30°C. The pink colonies of *Shewanella oneidensis* MR-1 was transferred to both a LB agar plates containing 15 mg L^{-1} gentamicin and a NaCl-less LB plates containing 10% sucrose. The two plates were incubated for 12-16 h at 30°C. The clones that grow on gentamicin-containing plates but not on sucrose plates were picked to colony PCR by using LF/SR and LR/SF as primers (Supplementary Table 2 and Supplementary Fig. 2a). The right clone that shows a wild-type band and a deletion band but not same. The right clone was transferred to NaCl-free LB without antibiotics and grown for 16 hours at 30°C. Then, the cells were transferred into fresh NaCl-free LB at a 1:100 dilution and cultured at 30°C until OD_{600} reached 0.4–0.6. The culture was diluted 10^{-2} and coated 100 μL onto NaCl-less while containing 10% sucrose LB plate. Pink clones were observed after incubating for 16 h at 30°C, and 20 clones were transferred to both a LB agar plates containing 15 mg L^{-1} gentamicin and a NaCl-less LB plates containing 10% sucrose. The clones that grew on NaCl-less LB plates containing 10% sucrose and did not grow on plates containing 15 mg L^{-1} gentamicin were picked to colony PCR by using LF/LR as primers (Supplementary Table 2 and Supplementary Fig. 2b). The positive clones were further confirmed by sequencing.

Construction of expression plasmid

For construction of expression plasmid pHG102-fdhAB, the gene fragment containing non-coding region including promoter, *fdhT* (So_4507), *fdhX* (*So*_4508), *fdhA* (*So*_4509) and *fdhB* (*So*_4510) was amplified by using genome of *Shewanella oneidensis* MR-1 as template and fdhA-F and fdhB-R as primers, and 25 μL PrimeSTAR Max DNA Polymerase was adding to a 50 μL volume of PCR system, followed by the PCR protocol: 98°C for 2 min (1 cycle); 98°C for 30 s; 52°C for 20 s; 72°C for 2 min (25 cycles); and 72°C for 10 min (1 cycle). The plasmid skeleton of pHG102 was amplified by using pHG102-F and pHG102-R as primers and PHG102 (A gift from gifts from Prof. Liu) as template, followed by the PCR steps: 98°C for 2 min (1 cycle); 98°C for 30 s; 52°C for 20 s; 72°C for 2 min (25 cycles); and 72 °C for 10 min (1 cycle). The methylated templates were specifically degraded by *Dpn*I. Both PCR products were purified by using DNA purification and recovery kit (TIANGEN, China, Beijing). The two purified PCR products were linked with a ClonExpress-II one-step cloning kit (37°C, 30 min). The linked product was transformed into *E. coli* TOP10 competent cells, and the cells were coated onto LB agar plates containing 50 mg L^{-1} kanamycin for growing 12

h at 37°C. For expression plasmid pHG102-fdhA, the gene fragment containing non-coding region including promoter, *fdhT* (So_4507), *fdhX* (So_4508), *fdhA* (So_4509) was amplified by using genome of *Shewanella oneidensis* MR-1 as template and fdhA-F and fdhA-R as primers.

For preparation of electrocompetent cells of *Shewanella oneidensis* MR-1Δ*fdhAB*. The *Shewanella oneidensis* MR-1Δ*fdhAB* strain was cultured in LB reached OD_{600} of 1.0 at 30°C, and 100 mL culture was centrifugated at 3000 x g, 4°C to collect cells. The cells were washed twice with 50 mL L-sorbitol (1M) pre-cooled at 4°C, followed resuspended with 5 mL L- sorbitol (1 M). 100 μL of competent cells was aliquoted into each tube pre-cooled at 4°C. A total of 200 ng of pHG102-fdhAB and pHG102-fdhA plasmids were added to *Shewanella oneidensis* MR-1Δ*fdhAB* competent cells and electrically transformed using a MicroPulser electroporator (BIO-RAD). The positive clones were selected from LB agar plates containing 50 mg L^{-1} kanamycin after culturing 12 h at 30°C.

Protein expression and purification

*So*FdhAB and *So*FdhA were expressed in *Shewanella oneidensis* MR-1Δ*fdhAB*. The *Shewanella oneidensis* MR-1Δ*fdhAB* grew in medium containing 10 g L^{-1} NaCl, 10 g L^{-1} peptone, 5 g L^{-1} Yeast extract, 40 mM fumaric acid, 0.5 mM Na_2WuO_4, 1 mM $NaNO_3$ and 20 mM DL-lactic acid, pH 7.4. 0.5 mM $FeSO_4$ was added when the OD_{600} reached 0.6~0.8, and cells were cultured for 20 h at 30°C, 150 rpm. The cells were collected by centrifugation with 5000 x g, 15 min, and washed once with buffer (0.1 M Tris-HCl, 0.3 M NaCl, pH 8.0). Cells were suspended with buffer (0.1 M Tris-HCl, 0.3 M NaCl, pH 8.0) containing 40 mg L^{-1} PMSF, and disrupted by ATS high-pressure homogenizer. The cell debris was removed by centrifugation with 17500 x g, 30 min, 4°C. The supernatant was mixed with 10 mM imidazole, and the mixture was passed twice through the Ni-NTA column, which was balanced by five column volumes of buffer (0.1 M Tris-HCl, 0.3 M NaCl, pH 8.0). The 100 mL buffer (0.1 M Tris-HCl, 0.3 M NaCl, pH 8.0) containing 50 mM imidazole was used for washing column. The target proteins were eluted with 10 mL of buffer (0.1 M Tris-HCl, 0.3 M NaCl, pH 8.0) containing 250 mM imidazole. Proteins were further purified by protein purifier (AKTA purifier, Cytiva) equipped with Superdex 200 (10/300 GL, Cytiva). The buffer (0.1 M Tris-HCl, 0.1 M NaCl, pH 8.0) flowed at a rate of 0.6 mL min^{-1}, and 0.25 mL of eluent was collected per tube. For anaerobic expression and purification, anaerobic expression was performed in anaerobic shake flask, and purification progress was carried out in anaerobic chamber (O_2<1 ppm) (Vigor Gas Purification Technologies Company, China Suzhou). The proteins were analyzed by 12% polyacrylamide gels and stained with Coomassie brilliant blue G250. The concentration of protein was measured by Bradford

method.

Metal content analysis

The protein used for metal content analysis was expressed in the above medium containing an additional 0.5 mM Na_2MoO_4. The molybdenum (Mo), tungsten (W) and iron (Fe) content in the *So*FdhAB was analyzed through ICP-MS (Perkin Elmer, USA) by Beijing Zhongke Baice Technology Service Co., Ltd.

Enzyme activity assay

Enzyme activity assay was performed in anaerobic chamber (O_2<1 ppm). For CO_2 reduction, reduced methyl viologen (MV^+) was prepared by reducing methyl viologen (MV^{2+}) through sodium dithionite (DTH). Buffer (0.1 M HEPES/NaOH, pH 7.0) was used for reaction. 2 mL reaction system containing 0.1 mM MV^+, 20 mM $NaHCO_3$. The decrease in absorption at 604 nm (ε = 13.9 mM^{-1} cm^{-1}) was monitored at 30°C using an Evolution One spectrophotometer (Thermo Fisher Scientific) equipped with a temperature control module after the addition of enzyme. One unit of CO_2 reduction activity was defined as the reduction of 1 μmol of CO_2 (corresponding to the oxidation of 2 μmol of MV^+) per minute under the assay conditions.

For formate oxidation, 2 mL reaction system containing 20 mM formate and 20 mM methyl viologen (MV^{2+}) used for electron acceptor. Similarly, the increased in absorption at 604 nm (ε = 13.9 mM^{-1} cm^{-1}) was monitored at 30°C after adding enzyme. One unit of formate oxidation activity was defined as the oxidation of 1 μmol of formate (corresponding to the reduction of 2 μmol of MV^{2+}) per minute.

Cryo-EM analysis of *So*FdhAB

The fresh protein with a concentration of 0.5 g L^{-1} was dropped (3 μL) onto a holey-carbon cryo-EM grids (Cu 300 mesh, QUANTIFOIL). Cryo-EM data were collected at Institute of Modern Agriculture, Peking University. Micrographs were acquired on a Titan Krios G4 (Thermo Fisher Scientific) microscope operating at 300 kV (Cs = 2.7 mm), equipped with a Gatan K3 detector. A calibrated magnification of 105 k was used, corresponding to a pixel size of 0.85 Å under super resolution mode. The defocus range was set between -1.6 μm and -2.6 μm. Each micrograph was dose-fractionated into 32 frames, and a cumulative dose of 50 e^- $Å^{-2}$ (Supplementary Table 3). MotionCor2 was used for motion correction and dose-weighting of frames. CTFFIND4.1 was employed to estimate the contrast transfer function (CTF) parameters from the motion-corrected micrographs. All subsequent image processing was performed in RELION3.1. A total of 9,000

micrographs were collected. Approximately 18179123 particles were auto-picked for initial 2D classification. A subset of 3768418 selected particles was using for 3D classification (Supplementary Table 3). These particles underwent 3D refinement imposing C1 symmetry, followed by Bayesian polishing. The final 3D reconstruction using 138699 polished particles yielded a map at 2.75 Å resolution (FSC = 0.143). The structure model was subsequently built and refined against the electron density by COOT. Molecular structure of *So*FdhAB visualization was performed using PYMOL, and the substrate channel prediction was carried out using the Caver 3.0.3 plugin. AlphaFold 3.0 was used to replenish the residue in FdhB subunit that were not observed due to insufficient resolution, when analyzing the mutation sites in the surface of FdhB that interacts with electrode interface.

Electrochemical experiments

The electrochemical experiments of *So*FdhAB were performed by potentiostat (CHI660e) and a rotating disk electrode (PINE). A three-electrode system was used, consisting of a glassy carbon electrode (0.07 cm^2) as the working electrode, a platinum sheet electrode (1 cm^2) as the counter electrode, and an Ag/AgCl electrode as the reference electrode. The glassy carbon electrode was polished with an alumina slurry (0.05 μm) on a polishing cloth, then sonicated three times for 1 min each in deionized water and once in ethanol. Carbon nanotube (CNT) was dispersed in water and dimethylformamide (DMF) (ratio of 1:1) to a concentration of 1 g L^{-1}. The carbon nanotube doped with 10 mM pyrene methylamine was prepared by adding 10 mM pyrene methylamine into Carbon nanotube (CNT) with a concentration of 1 g L^{-1}, following by ultrasonic treatment for 2 hours. A CNT/GC electrode was fabricated by drop-casting two layers of CNT dispersion (5 μL per layer) onto a polished GC electrode, with intermediate drying at 60°C for 20 min between layers. For bioelectrodes construction, 10 μL of enzyme (1.5 g L^{-1}) was adding onto CNT/GC electrode, and followed was left to stand at 4°C for 6 h. The excess enzyme solution was gently removed, and the electrode was washed by buffer (0.1 M HEPES/NaOH, 0.1 M NaCl, pH 7.0) before testing. All applied potentials were converted to the standard hydrogen electrode (SHE) reference using equation 1 at 25°C and pH 7.0.

$$E\ (SHE) = E\ (Ag/AgCl) + 0.197 \quad (1)$$

The scan rate of Cyclic voltammetry (CV) was 10 mV s^{-1}, while the scan rate of linear sweep voltammetry (LSV) was 1 mV s^{-1}. CV and LSV analysis were performed at 25°C in 0.1 M HEPES/NaOH, 0.1 M NaCl, pH 6.2. For the pH-dependence experiment, pH was controlled using a mixed buffer [100 mM acetate, 2-morpholinoethanesulfonic acid (MES), N-cyclohexyl-2-

aminoethanesulfonic acid (HEPES), and N-tris(hydroxymethyl)methyl-3-aminopropanesulfonic acid (TAPS)] and verified after experimentation.

Molecular dynamics (MD) simulations of enzyme−electrode interaction

For MD simulations, the model of *So*FdhAB-Y94S was built by AphFold 3.0. CNTs (100, 0, three-walled) with a diameter of approximately 9.5 nm and a length of 6.0 nm were constructed using Nanotube Modeler[64]. The interlayer spacing was set to 0.34 nm [65]. For all simulation systems, a simplified CNT model with dimensions of 60 Å × 60 Å containing 4617 carbon atoms was used, and the CNT atoms were kept fixed during the simulations[58]. All MD simulations were performed using GROMACS 2023.2. The GROMOS 54A7 force field was selected based on its demonstrated reliability for modeling biomolecules and CNT systems[66]. System preparation followed a consistent protocol, including energy minimization and equilibration under NVT and NPT ensembles. Three independent MD production runs (100 ns each) were performed for each system using different initial atomic velocities to avoid sampling artifacts[67]. To ensure a consistent starting configuration, both *So*FdhAB-WT and *So*FdhAB-Y94S were placed above the CNT surface with identical initial orientations and at an initial separation of 6.5 Å from the nanotube. Each system was solvated with approximately 38000 SPCE water molecules within a periodic simulation box. The distances between distal Fe-S cluster and CNT were analyzed using built-in GROMACS tools. Structural snapshots illustrating the biomolecule-CNT interaction process and distance measurements were rendered using PyMOL v3.1.3.

Average coverage analysis

The average coverage (Γ) of enzyme on electrodes was quantified by detecting the non-turnover redox peaks (NTPs). The bioelectrode was constructed in the same way as in the catalytic experiment that 10 μL of enzyme (1.5 g L^{-1}) was adding onto CNT/GC electrode (0.07 cm^2), and incubated at 4°C for 6 h. The excess enzyme solution was gently removed, and the electrode was washed by buffer (0.1 M HEPES/NaOH, 0.1 M NaCl, pH 7.0) before testing. The non-turnover redox peaks (NTPs) of *So*FdhAB and *So*FdhAB-Y94S was detected using buffer (0.1 M HEPES/NaOH, 0.1 M NaCl, pH 7.0) as electrolyte in an anaerobic chamber (O_2<1 ppm, 100% N_2). The non-turnover redox peaks were tested under different scan rate, and the average coverage was calculated through following formula. The formula (4) was obtained from formula (2) and (3).

$$Ip = nFQv/4RT \quad (2)$$

$$\Gamma = Q/nFA \quad (3)$$

$$Ip = n^2F^2A\Gamma v/4RT \quad (4)$$

Ip peak current, A

n electron transfer number, 1

F=96485 C mol^{-1}

Γ average coverage, mol cm^{-2}

Q The electrical charge during the electron transfer process, C

v scan rate V s^{-1}

R=8.314 J·mol^{-1}·K^{-1}

T=298.15 K

A electrode area, 0.07 cm^2

Bioelectrocatalytic synthesis formate from CO_2

A carbon paper (TORAY, Japan) with area of 1 cm^2 was used for constructing work electrode. A total of 100 μL of NH_2-CNT (1 g L^{-1}) was added onto carbon paper and dried at 60°C to form a NH_2-CNT/CP electrode. After cooling, 100 μL of *So*FdhAB-Y94S (1.5 g L^{-1}) was dropped onto the CNT/CP electrode and left to stand for 6 h at 4°C to construct the *So*FdhAB-Y94S/NH_2-CNT/CP electrode. The excess enzyme solution was gently removed. Three electrodes system mentioned above including *So*FdhAB-Y94S/NH_2-CNT/CP electrode (1 cm^2), platinum sheet electrode (1 cm^2) and Ag/AgCl electrode were used. Chronoamperometry was carried out in 5 mL of electrolyte (0.1 M HEPES/NaOH, 0.1 M NaCl, pH 7.0) respectively under CO_2, mixed gas (10% CO_2+20% O_2+70% N_2) and syngas (40% CO_2+40% CO+20% H_2), and a continuous flow of 20 sccm and a constant voltage of −600 mV *vs.* SHE was used.

For the bioelectrocatalytic CO_2 reduction in H-cell, *So*FdhAB-Y94S/NH_2-CNT/CP was used as work electrode in cathode chamber, which also was equipped with Ag/AgCl electrode as reference electrode. Anode chamber was equipped with a platinum sheet (1 cm^2) as counter electrode. The anode chamber and the cathode chamber are separated by a proton exchange membrane (N212). Chronoamperometry was carried out in 10 mL of electrolyte (0.1 M HEPES/NaOH, 0.1 M NaCl, pH 7.0) respectively under CO_2 with continuous flow of 20 sccm and a constant voltage of −600 mV *vs.* SHE was used. The formate concentration in cathode chamber was detected.

The formate concentration in the electrolyte was determined using high-performance liquid chromatography (HPLC) equipped with a RID-20A detector (Nexera XR, Shimadzu) and an Aminex HPX-87H column (300 × 7.8 mm, Bio-Rad). The mobile phase was 5 mM H_2SO_4, with a flow rate

of 0.6 mL min^{-1} and a column temperature of 60 °C. All samples were prepared by adding H_2SO_4 to a final concentration of 5 mM and then centrifuged at 12,000 × g for 10 min. A standard curve for formate was generated using known concentrations ranging from 1 to 100 mM. The faraday efficiency (FE) was calculated according to equation 5.

$$FE\ (\%) = \frac{Q\ (formate)}{Q\ (tot)} * 100\% = \frac{c\ (formate) * V * Z * F}{j * t} \quad (5)$$

where *c (formate)* is the formate concentration after reaction time t (s), *V* is the volume of the electrolyte, *z* is the number of electrons required to reduce CO_2 to formate, and the value is 2, *F* is the Faraday constant (96,485 C mol^{-1}), and *j* is the recorded current.

Data availability

The structural model of *So*FdhAB has been deposited in the Protein Data Bank (PDB) with accession codes 9VAP [https://www.rcsb.org/structure/unreleased/9VAP]. Protein structures of *Ec*FDH-H, PDB ID 1FDI [https://www.rcsb.org/structure/1FDI], *Tk*HDCR, PDB ID 7QV7 [https://www.rcsb.org/structure/7QV7] and *Dv*H-FDH, PDB ID 6SDR [https://www.rcsb.org/structure/6SDR] are available from the PDB. The genomic data of *Shewanella oneidensis* MR-1 are available from the National Center for Biotechnology Information (NCBI) database [https://www.ncbi.nlm.nih.gov/nuccore/AE014299.2]. All relevant data generated and analyzed during this study which include enzyme activity assay and electrochemical data are included in this article and its supplementary information. Source data are provided with this paper.

References

1. Liu, Z. Wang, K. Chen, Y. Tan, T. Nielsen, J. Third-generation biorefineries as the means to produce fuels and chemicals from CO_2. *Nat. Catal.* **3,** 274-288 (2020).

2. Gleizer, S. et al. Conversion of *Escherichia coli* to generate all biomass carbon from CO_2. *Cell* **179,** 1255-1263.e1212 (2019).

3. Cai, T. et al. Cell-free chemoenzymatic starch synthesis from carbon dioxide. *Science* **373,** 1523-1527 (2021).

4. Zheng, T. T. et al. Upcycling CO_2 into energy-rich long-chain compounds via electrochemical and metabolic engineering. *Nat. Catal.* **5,** 388-396 (2022).

5. Cui, H. et al. Converting CO_2 to single-cell protein via an integrated electrocatalytic-biosynthetic system. *Appl. Catal. B Environ.* **350,** 123946 (2024).

6. Wu, R. et al. Enzymatic Electrosynthesis of glycine from CO_2 and NH_3. *Angew. Chem. Int. Ed.* **62,**

(2023).

7. Fang, W. et al. Durable CO_2 conversion in the proton-exchange membrane system. *Nature* **626,** 86-91 (2024).

8. Contaldo, U. et al. Efficient electrochemical CO_2/CO interconversion by an engineered carbon monoxide dehydrogenase on a gas-diffusion carbon nanotube-based bioelectrode. *ACS Catal.* **11,** 5808-5817 (2021).

9. Cobb, S. J. et al. Fast CO_2 hydration kinetics impair heterogeneous but improve enzymatic CO_2 reduction catalysis. *Nat. Chem.* **14,** 417-424 (2022).

10. Reda, T. Plugge, C. M. Abram, N. J. Hirst, J. Reversible interconversion of carbon dioxide and formate by an electroactive enzyme. *Proc. Natl. Acad. Sci. U.S.A.* **105,** 10654-10658 (2008).

11. Robinson, W. E. Bassegoda, A. Reisner, E. Hirst, J. Oxidation-state-dependent binding properties of the active site in a Mo-containing formate dehydrogenase. *J. Am. Chem. Soc.* **139,** 9927-9936 (2017).

12. Robinson, W. E. Bassegoda, A. Blaza, J. N. Reisner, E. Hirst, J. Understanding how the rate of C–H bond cleavage affects formate oxidation catalysis by a Mo-dependent formate dehydrogenase. *J. Am. Chem. Soc.* **142,** 12226-12236 (2020).

13. Bassegoda, A. Madden, C. Wakerley, D. W. Reisner, E. Hirst, J. Reversible interconversion of CO_2 and formate by a molybdenum-containing formate dehydrogenase. *J Am Chem Soc* **136,** 15473-15476 (2014).

14. Li, W. et al. Direct detection of a single [4Fe-4S] cluster in a tungsten-containing enzyme: electrochemical conversion of CO_2 into formate by formate dehydrogenase. *Carbon Energy* **5,** e304 (2023).

15. Chen, H. et al. Fundamentals, Applications, and future directions of bioelectrocatalysis. *Chem. Rev.* **120,** 12903-12993 (2020).

16. Karyakin, A. A. et al. The limiting performance characteristics in bioelectrocatalysis of hydrogenase enzymes. *Angew. Chem. Int. Ed.* **46,** 7244-7246 (2007).

17. Wang, Y. Kang, Z. Zhang, L. Zhu, Z. Elucidating the interactions between a [NiFe]-hydrogenase and carbon electrodes for enhanced bioelectrocatalysis. *ACS Catal.* **12,** 1415-1427 (2022).

18. Becker, J. M. et al. Bioelectrocatalytic CO_2 reduction by redox polymer-wired carbon monoxide dehydrogenase gas diffusion electrodes. *ACS Appl. Mater. Interfaces* **14,** 46421-46426 (2022).

19. Parkin, A. Seravalli, J. Vincent, K. A. Ragsdale, S. W. Armstrong, F. A. Rapid and efficient

electrocatalytic CO_2/CO interconversions by carboxydothermus hydrogenoformans CO dehydrogenase I on an electrode. *J. Am. Chem. Soc.* **129,** 10328-10329 (2007).

20. Contaldo, U. et al. Efficient electrochemical CO_2/CO interconversion by an engineered carbon monoxide dehydrogenase on a gas-diffusion carbon nanotube-based bioelectrode. *ACS Catal.* **11,** 5808-5817 (2021).

21. Hirst, J. Elucidating the mechanisms of coupled electron transfer and catalytic reactions by protein film voltammetry. *Biochim. Biophys. Acta (BBA) - Bioenergetics* **1757,** 225-239 (2006).

22. Zu, Y. Fee, J. A. Hirst, J. Breaking and re-forming the disulfide bond at the high-potential, respiratory-type rieske [2Fe-2S] center of thermus thermophilus: Characterization of the sulfhydryl state by protein-film voltammetry. *Biochemistry* **41,** 14054-14065 (2002).

23. Zu, Y. et al. Reduction potentials of rieske clusters: Importance of the coupling between oxidation state and histidine protonation state. *Biochemistry* **42,** 12400-12408 (2003).

24. Badiani, V. M. et al. Elucidating film loss and the role of hydrogen bonding of adsorbed redox enzymes by electrochemical quartz crystal microbalance analysis. *ACS Catal.* **12,** 1886-1897 (2022).

25. Chemla, Y. Kaufman, F. Amiram, M. Alfonta, L. Expanding the genetic code of bioelectrocatalysis and biomaterials. *Chem. Rev.* **124,** 11187-11241 (2024).

26. Badiani, V. M. et al. Engineering electro- and photocatalytic carbon materials for CO_2 reduction by formate dehydrogenase. *J. Am. Chem. Soc.* **144,** 14207-14216 (2022).

27. Alvarez-Malmagro, J. et al. Bioelectrocatalytic activity of W-formate dehydrogenase covalently immobilized on functionalized gold and graphite electrodes. *ACS Appl. Mater. Interfaces.* **13,** 11891 (2021).

28. Liu, W. et al. Bioelectrocatalytic carbon dioxide reduction by an engineered formate dehydrogenase from *Thermoanaerobacter kivui*. *Nat. Commun.* **15,** 9962 (2024).

29. Schwarz, F. M. Schuchmann, K. Muller, V. Hydrogenation of CO_2 at ambient pressure catalyzed by a highly active thermostable biocatalyst. *Biotechnol. Biofuels* **11,** 237 (2018).

30. Dietrich, H. M. et al. Membrane-anchored HDCR nanowires drive hydrogen-powered CO_2 fixation. *Nature* **607,** 823-830 (2022).

31. Schuchmann, K. Müller, V. Direct and reversible hydrogenation of CO_2 to formate by a bacterial carbon dioxide reductase. *Science* **342,** 1382-1385 (2013).

32. de Bok, F. A. et al. Two W-containing formate dehydrogenases (CO_2-reductases) involved in syntrophic propionate oxidation by *Syntrophobacter fumaroxidans*. *Eur J Biochem* **270,** 2476-2485

(2003).

33. Böhmer, N. Hartmann, T. Leimkühler, S. The chaperone FdsC for Rhodobacter capsulatus formate dehydrogenase binds the bis-molybdopterin guanine dinucleotide cofactor. *FEBS Letters* **588,** 531-537 (2014).

34. Iliuta, I. Larachi, F. Direct-air capture conversion of CO_2 in fixed-bed microreactors with immobilized formate dehydrogenase and glucose dehydrogenase: Concept feasibility. *Chem. Eng. Res. Des.* **193,** 306-319 (2023).

35. Min, K. et al. Elevated conversion of CO_2 to versatile formate by a newly discovered formate dehydrogenase from *Rhodobacter aestuarii*. *Bioresour. Technol.* **305,** 123155 (2020).

36. Brouwer, E.-M. et al. Characterization of the oxygen-tolerant formate dehydrogenase from *Clostridium carboxidivorans*. *Front. Microbiol.* **15,** 1527626, (2025).

37. Yoshikawa, T. et al. Multiple electron transfer pathways of tungsten-containing formate dehydrogenase in direct electron transfer-type bioelectrocatalysis. *Chem. Commun.* **58,** 6478-6481 (2022).

38. Jeon, B. W. et al. Enzymatic conversion of CO_2 to formate: The potential of tungsten-containing formate dehydrogenase in flow reactor system. *J. CO_2 Util.* **82,** 102754 (2024).

39. Cha, J. Lee, J. Jeon, B. W. Kim, Y. H. Kwon, I. Real flue gas CO_2 hydrogenation to formate by an enzymatic reactor using O_2- and CO-tolerant hydrogenase and formate dehydrogenase. *Front. Bioeng. Biotechnol.* **11,** 1265272, (2023).

40. Lee, J. et al. Molar-scale formate production via enzymatic hydration of industrial off-gases. *Nat. Chem. Eng.* **1,** 354-364 (2024).

41. Fera, M.-C. et al. Bioelectrocatalytic CO_2 reduction to formate by *Candida boidinii* formate dehydrogenase overcoming NADH dependence with tailored amino-viologen redox polymers. *J. CO_2 Util.* **93,** 103041 (2025).

42. Oliveira, A. R. et al. Toward the mechanistic understanding of enzymatic CO_2 reduction. *ACS Catal.* **10,** 3844-3856 (2020).

43. Kuk, S. K. et al. NADH-free electroenzymatic reduction of CO_2 by conductive hydrogel-conjugated formate dehydrogenase. *ACS Catal.* **9,** 5584-5589 (2019).

44. Oliveira, A. R. et al. An allosteric redox switch involved in oxygen protection in a CO_2 reductase. *Nat. Chem. Biol.* **20,** 111-119 (2024).

45. Yu, T. et al. Enzyme function prediction using contrastive learning. *Science* **379,** 1358-1363

(2023).

46. Wang, Z. et al. Robust enzyme discovery and engineering with deep learning using CataPro. *Nat. Commun.* **16,** 2736 (2025).

47. Li, Y. et al. Metabolic regulation of *Shewanella oneidensis* for microbial electrosynthesis: From extracellular to intracellular. *Metab. Eng.* **80,** 1-11 (2023).

48. Brondino, C. D. et al. Incorporation of either molybdenum or tungsten into formate dehydrogenase from *Desulfovibrio alaskensis* NCIMB 13491: EPR assignment of the proximal iron-sulfur cluster to the pterin cofactor in formate dehydrogenases from sulfate-reducing bacteria. *J. Biol. Inorg. Chem.* **9,** 145-151 (2004).

49. Maia, L. B. Fonseca, L. Moura, I. Moura, J. J. G. Reduction of carbon dioxide by a molybdenum-containing formate dehydrogenase: A kinetic and mechanistic study. *J. Am. Chem. Soc.* **138,** 8834-8846 (2016).

50. Cobb, S. J. Dharani, A. M. Oliveira, A. R. Pereira, I. A. C. Reisner, E. Carboxysome-inspired electrocatalysis using enzymes for the reduction of CO_2 at low concentrations. *Angew. Chem., Int. Ed.* **62,** e202218782 (2023).

51. Yang, J. Y. Kerr, T. A. Wang, X. S. Barlow, J. M. Reducing CO_2 to HCO_2^- at mild potentials: lessons from formate dehydrogenase. *J. Am. Chem. Soc.* **142,** 19438-19445 (2020).

52. Steinhilper, R. Höff, G. Heider, J. Murphy, B. J. Structure of the membrane-bound formate hydrogenlyase complex from *Escherichia coli*. *Nat. Commun.* **13,** 5395 (2022).

53. Page, C. C. Moser, C. C. Chen, X. X. Dutton, P. L. Natural engineering principles of electron tunnelling in biological oxidation-reduction. *Nature* **402,** 47-52 (1999).

54. Cellini, A. et al. Directed ultrafast conformational changes accompany electron transfer in a photolyase as resolved by serial crystallography. *Nat. Chem.* **16,** 24 (2024).

55. Winkler, J. R. Gray, H. B. Long-range electron tunneling. *J. Am. Chem. Soc.* **136,** 2930-2939 (2014).

56. Kurisu, G. et al. Structure of the electron transfer complex between ferredoxin and ferredoxin-$NADP^+$ reductase. *Nat. Struct. Biol.* **8,** 117-121 (2001).

57. Volbeda, A. Darnault, C. Renoux, O. Nicolet, Y. Fontecilla-Camps, J. C. The crystal structure of the global anaerobic transcriptional regulator FNR explains its extremely fine-tuned monomer-dimer equilibrium. *Sci. Adv.* **1,** e1501086 (2015).

58. Cui, H. et al. Rapid and oriented immobilization of laccases on electrodes via a methionine-rich

peptide. *ACS Catal.* **11,** 2445-2453 (2021).

59. Boyington, J. C. Gladyshev, V. N. Khangulov, S. V. Stadtman, T. C. Sun, P. D. Crystal structure of formate dehydrogenase H: catalysis involving Mo, molybdopterin, selenocysteine, and an Fe_4S_4 cluster. *Science* **275,** 1305-1308 (1997).

60. Edwardes Moore, E. et al. Understanding the local chemical environment of bioelectrocatalysis. *Proc. Natl. Acad. Sci. U.S.A.* **119,** e2114097119 (2022).

61. Nguyen, L.-T. Schmidt, H. A. von Haeseler, A. Minh, B. Q. IQ-TREE: A fast and effective stochastic algorithm for estimating maximum-likelihood phylogenies. *Mol. Biol. Evol.* **32,** 268-274 (2014).

62. Letunic, I. Bork, P. Interactive Tree of Life (iTOL) v6: recent updates to the phylogenetic tree display and annotation tool. *Nucleic Acids Res.* **52,** 78-82 (2024).

63. Jin, M. et al. Unique organizational and functional features of the cytochrome c maturation system in *Shewanella oneidensis*. *PLoS ONE* **8,** e75610 (2013).

64. Melchor, S. Dobado, J. A. CoNTub: An algorithm for connecting two arbitrary carbon nanotubes. *J. Chem. Inf. Comput. Sci.* **44,** 1639-1646 (2004).

65. Li, C. Chou, T.-W. Elastic moduli of multi-walled carbon nanotubes and the effect of van der Waals forces. *Compos. Sci. Technol.* **63,** 1517-1524 (2003).

66. Wang, H. Michielssens, S. Moors, S. L. C. Ceulemans, A. Molecular dynamics study of dipalmitoylphosphatidylcholine lipid layer self-assembly onto a single-walled carbon nanotube. *Nano Res.* **2,** 945-954 (2009).

67. Zhang, M. et al. Engineering a binding peptide for oriented immobilization and efficient bioelectrocatalytic oxygen reduction of multicopper oxidases. *ACS Appl. Mater. Interfaces* **17,** 2355-2364 (2025).

68. Edwardes Moore, E. et al. A Semi-artificial photoelectrochemical tandem leaf with a CO_2-to-formate efficiency approaching 1%. *Angew. Chem., Int. Ed.* **60,** 26303 (2021).

69. Miller, M. et al. Interfacing formate dehydrogenase with metal oxides for the reversible electrocatalysis and solar-diven reduction of carbon dioxide. *Angew. Chem., Int. Ed.* **58,** 4601-4605 (2019).

Acknowledgement

This study was supported by Strategic Priority Research Program of the Chinese Academy of

Sciences (XDC0120103 to L. Z.), Coal-Major Project (2025ZD1701600 to L. Z.), the Tianjin Science Fund for Distinguished Young Scholars (22JCJQJC00100 to Z. Z.), and the International Partnership Program of Chinese Academy of Sciences, Grant No. 306GJHZ2025003BS to L. Z.. We are grateful to Professor Shenghai Chang for his supervision in structural analysis, and to Dr. Tailin Wang for insightful discussions.

Author contributions

Experiment, data analysis and writing the initial manuscript were performed by W. L.. P. Z. preformed the bioinformatics analysis. Molecular dynamics (MD) simulation was performed by X. W., and H. C. (Haiyang Cui) provided supervision. Cryo-EM analysis was supervised by K. Z., W. Y. and C. Y.. Electrochemical experiments were supervised by H. C. (Huijuan Cui). Data analysis and biochemistry experiments were supervised by C. Y., Z. Z. and J. S.. J. L. provide experimental materials. Project conception, fund support, overall supervision and writing paper were performed by L. Z..

Competing interests

The authors declare no competing interests.

Table 1. Comparison of electrocatalytic CO_2 reduction via direct electron transfer by Mo/W-containing FDHs.

Enzymes	**Electrode modification**	**Potential/V vs. SHE**	**Current density/μA cm^{-2}**	**Electrode area/cm^2**	**Production rate /μmol h^{-1}cm^{-2}**	**Oxygen sensitivity**	**References**
*Sf*FDH-1	Pyrolytic graphite electrode	-0.8	-80	-	-	Irreversible oxygen deactivation	10
*Ec*FDH	Pyrolytic graphite electrode	-0.6	-200	-	-	Irreversible oxygen deactivation	13
*Cl*FDH	Pyrolytic graphite electrode	-0.8	-400	-	-	Reversible oxygen deactivation	14
*Dv*H-FDH	IO-TiO_2 I Perovskite I $BIVO_4$		-5000	0.19	7	Reversible oxygen deactivation	68
*Dv*H-FDH	IO-TiO_2	-0.6	-800	0.19	10[a]	Reversible oxygen deactivation	60
*Dv*H-FDH	MesoTiO_2 electrode	-0.6	-100	0.25	0.82	Reversible oxygen deactivation	69
*Dv*H-FDH	$NHMe_2^+$ modified carbon nanotubes	-0.6	-247	0.07	1.2	Reversible oxygen deactivation	26
FdhF_HycB3Δ159-184	Carbon nanotubes	-0.5	-270	1.0	2.9	Irreversible oxygen deactivation	28
*So*FdhAB-Y94S	NH_2-carbon nanotubes	-0.6	-3100	1.0	45.3	Fully tolerant	This work

a *Dv*H-FDH is reported to achieve a rate of 55 μmol h^{-1}cm^{-2} at a higher overpotential (-0.8 V *vs.* SHE). The value listed in the table is for comparison in the same condition.

Fig. 1 The mining of formate dehydrogenase with high activity and oxygen tolerance. (a) Key steps for enzyme mining, (b) The phylogenetic analysis of candidate FDHs, (c) SDS-PAGE analysis of *So*FdhA and *So*FdhAB expressed in *Shewanella oneidensis* MR-1Δ*fdhAB*, (d) The k_{cat} of *So*FdhAB and *So*FdhA for CO_2 reduction, (e) The k_{cat} of *So*FdhAB and *So*FdhA for formate oxidation, *So*FdhAB* was expressed without Na_2WuO_4. The activity assay was performed in anaerobic chamber, and methyl viologen (MV) used for electron acceptor/donor, 20 mM $NaHCO_3$ and 20 mM formate are respectively used as substrates. The error bars correspond to the standard deviation of at least three independent measurements, and the center value for the error bars is the average of the three independent measurements. Source data are provided as a Source Data file.

Fig. 2 Electrocatalytic CO_2 reduction by *So*FdhAB. (a) LSVs of *So*FdhAB/CNT/GC electrode for CO_2 reduction on rotating disk electrode, (b) The bonding model of *So*FdhAB on different electrode materials, (c) Cyclic voltammetry (CV) of *So*FdhAB/CNT/GC electrode for CO_2 reduction, black line a: 100% N_2, red line b: saturated CO_2, blue line c: saturated CO_2 with 0.2 mM methyl viologen (MV) in the electrolyte, (d) The reduction current densities at -550 mV *vs.* SHE recorded at different electrodes in DET mode, (e) The IET efficiency of *So*FdhAB at different electrodes. All experiments were conducted in 0.1 M HEPES/NaOH, 0.1 M NaCl, pH 6.2, 25 ℃, the continuous CO_2 gas with flow rate of 20 sccm used as substrate, and the scan rate of CV was 10 mV s^{-1}, the scan rate of LSV was 1 mV s^{-1}, and the electrode rotation rate was 900 rpm unless specific statement. The error bars correspond to the standard deviation of at least three independent measurements, and the center value for the error bars is the average of the three independent measurements. Source data are provided as a Source Data file.

Fig. 3 The molecular basis of electrocatalysis by *So*FdhAB. (a) The electron transfer pathway consisted by [4Fe-4S] clusters in *So*FdhAB, (b) The overall structure of *So*FdhAB (PDB: 9VAP), (c) the interface interaction of subunit FdhA (wine red) and subunit FdhB (Cyan), (d) The interface around B4 Fe-S cluster, (e) The relative activities of *So*FdhAB-WT and four variants for CO_2 reduction, the activity assay was performed in anaerobic chamber, and reduced methyl viologen used for electron donor, 20 mM $NaHCO_3$ used as substrates, values are normalized to the *So*FdhAB-WT based on specific activity, (f) The relative DET-type current of CO_2 reduction of *So*FdhAB-WT and four variants at different modified electrodes, (g) The relative IET efficiency of *So*FdhAB-WT and four variants at different modified electrodes, (h) The structure of *Dv*H-FDH (PDB: 6SDR), (i) The structure of FdhF_HycB3Δ159-184 (PDB: 7QV7). All electrochemical experiments were

implemented in 0.1 M HEPES/NaOH, 0.1 M NaCl, pH 6.2, 25 ℃, the continuous CO_2 gas with flow rate of 20 sccm used as substrate, and the scan rate of CV was 10 mV s^{-1}, the electrode rotation rate was 900 rpm. The error bars correspond to the standard deviation of at least three independent measurements, and the center value for the error bars is the average of the three independent measurements. Source data are provided as a Source Data file.

Fig. 4. **The molecular mechanism of oxygen tolerance**. (a) The relative activity for CO_2 reduction of enzymes with (+) and without (−) preincubation with DTT, (b) The relative activity for formate oxidation of enzymes with (+) and without (−) preincubation with DTT, (c) The structure of *So*FdhAB (wine red) aligns with the structure of *Dv*H-FDH (deep blue), the proposed formate (Cyan) and CO_2 (Green) tunnels was showed in *So*FdhAB, (d) CO_2 reduction activity of *So*FdhAB and its variants expressed and purified under respectively under aerobic and anaerobic conditions, (e) Formate oxidation of *So*FdhAB and its variants expressed and purified under respectively under aerobic and anaerobic conditions. The DTT incubation experiment was conducted in an anaerobic chamber, and 2 mM DTT was added to 1 g L^{-1} protein solution and incubated at 4°C for 2 hours. The activity assay was performed in anaerobic chamber, and methyl viologen used for electron donor/acceptor, 20 mM $NaHCO_3$ and 20 mM formate used as substrates, values are normalized to the DTT-free control based on specific activity. The error bars correspond to the standard deviation of at least three independent measurements, and the center value for the error bars is the average of the three independent measurements. Source data are provided as a Source Data file.

Fig. 5 Electrosynthesis of formate from CO_2 catalyzed by *So*FdhAB-Y94S. (a) The cyclic voltammetry test of *So*FdhAB-Y94S under CO_2, (b) i-t curve under CO_2, the red arrow indicates the replacement of fresh electrolyte, (c) Time course of formate accumulation under CO_2, the red asterisk indicates the CO_2 reduction rate of *Dv*H-FDH at a potential of -0.6 V *vs.* SHE[60], (d) i-t curve catalyzed by *So*FdhAB-Y94S in H-cell, (e) Time course of formate accumulation in H-cell, (f) The cyclic voltammetry test of *So*FdhAB-Y94S mixed gas, (g) i-t curve under mixed gas, (h) Time course of formate accumulation under mixed gas, A potential of -600 mV *vs.* SHE was applied, the 0.1 M HEPES/NaOH, 0.1 M NaCl, pH 7.0 was used for i-t test, and the gas flow rate was 20 sccm, mixed gas:10% CO_2+20% O_2+70% N_2. The error bars correspond to the standard deviation of at least three independent measurements, and the center value for the error bars is the average of the three independent measurements. Source data are provided as a Source Data file.

Editorial Summary

Formate dehydrogenases (FDH) offer a route for carbon fixation but are limited by interfacial-intramolecular electron transfer (IIET) and oxygen sensitivity. Here the authors mine an FDH from S. oneidensis MR-1 featuring oxygen compatibility and direct-electron-transfer electrocatalytic performances.

Peer review information: *Nature Communications* thanks Cunduo Tang, and the other, anonymous, reviewer(s) for their contribution to the peer review of this work. A peer review file is available.

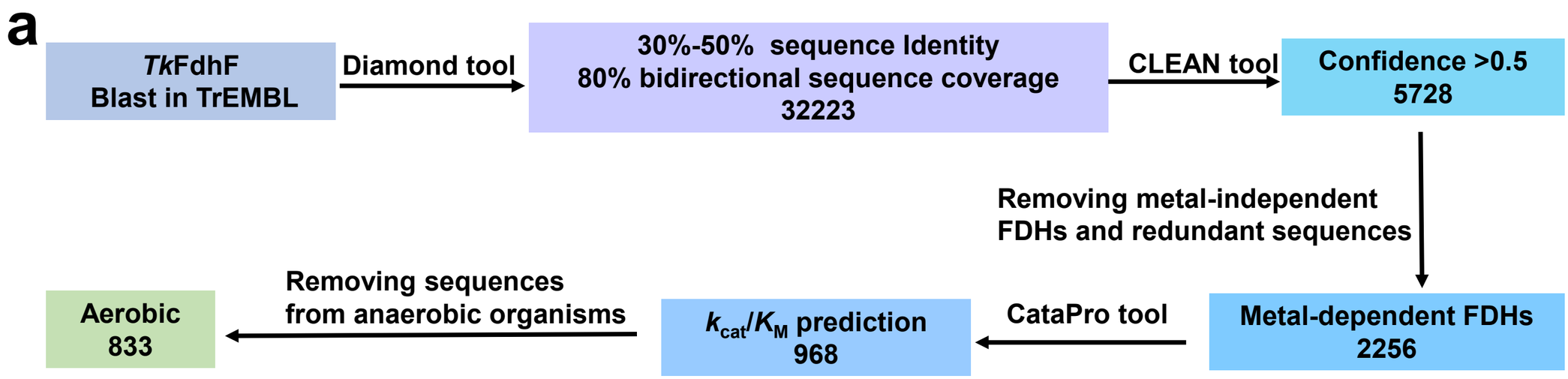
a
TkFdhF
Blast in TrEMBL
Diamond tool
30%-50% sequence Identity
80% bidirectional sequence coverage
32223
CLEAN tool
Confidence >0.5
5728
Removing metal-independent
FDHs and redundant sequences
Metal-dependent FDHs
2256
CataPro tool
kcat/KM prediction
968
Removing sequences
from anaerobic organisms
Aerobic
833

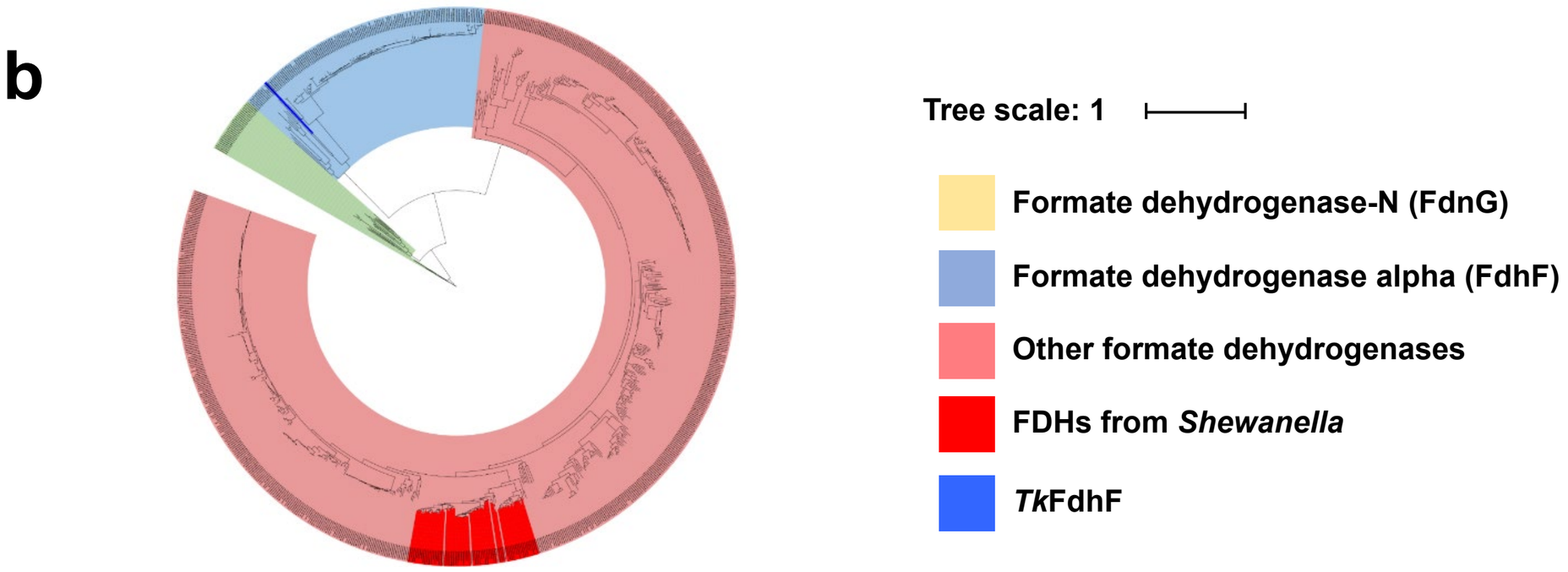
b
Tree scale: 1
Formate dehydrogenase-N (FdnG)
Formate dehydrogenase alpha (FdhF)
Other formate dehydrogenases
FDHs from Shewanella
TkFdhF

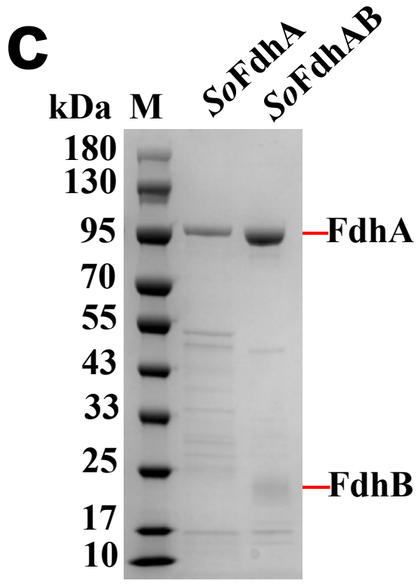
c
kDa
M
SoFdhA
SoFdhAB
180
130
95
70
55
43
33
25
17
10
FdhA
FdhB

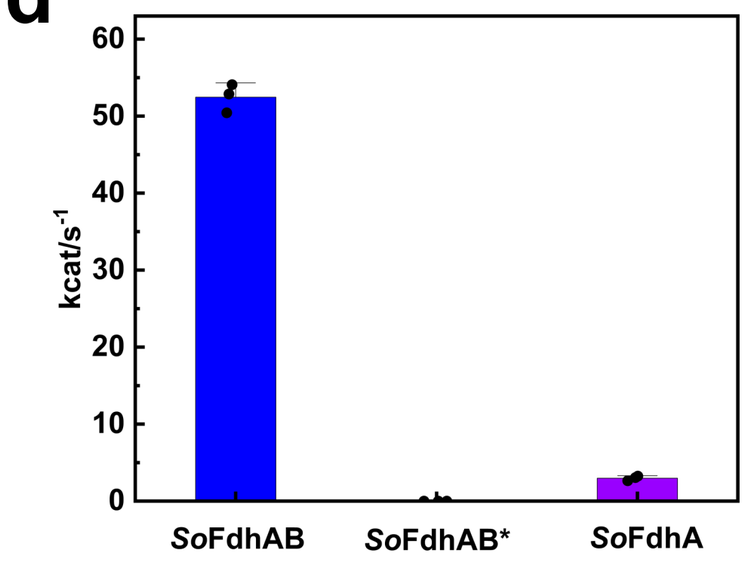
d
kcat/s-1
60
50
40
30
20
10
0
SoFdhAB
SoFdhAB*
SoFdhA

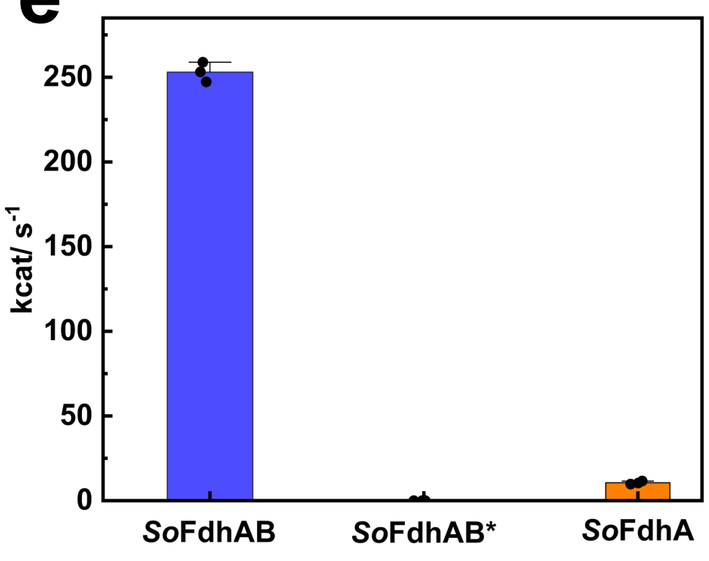
e
kcat/ s-1
250
200
150
100
50
0
SoFdhAB
SoFdhAB*
SoFdhA

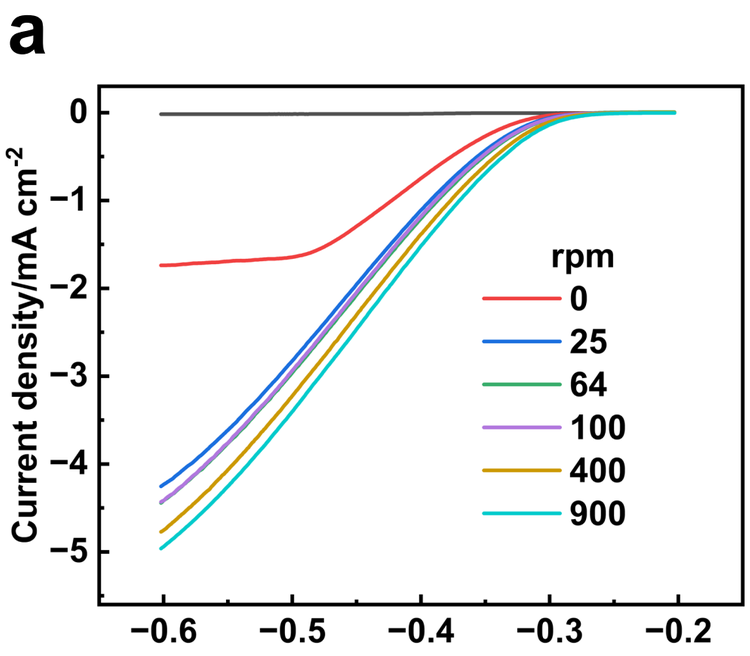
a
Current density/mA cm-2
0
−1
−2
−3
−4
−5
−0.6
−0.5
−0.4
−0.3
−0.2
rpm
0
25
64
100
400
900

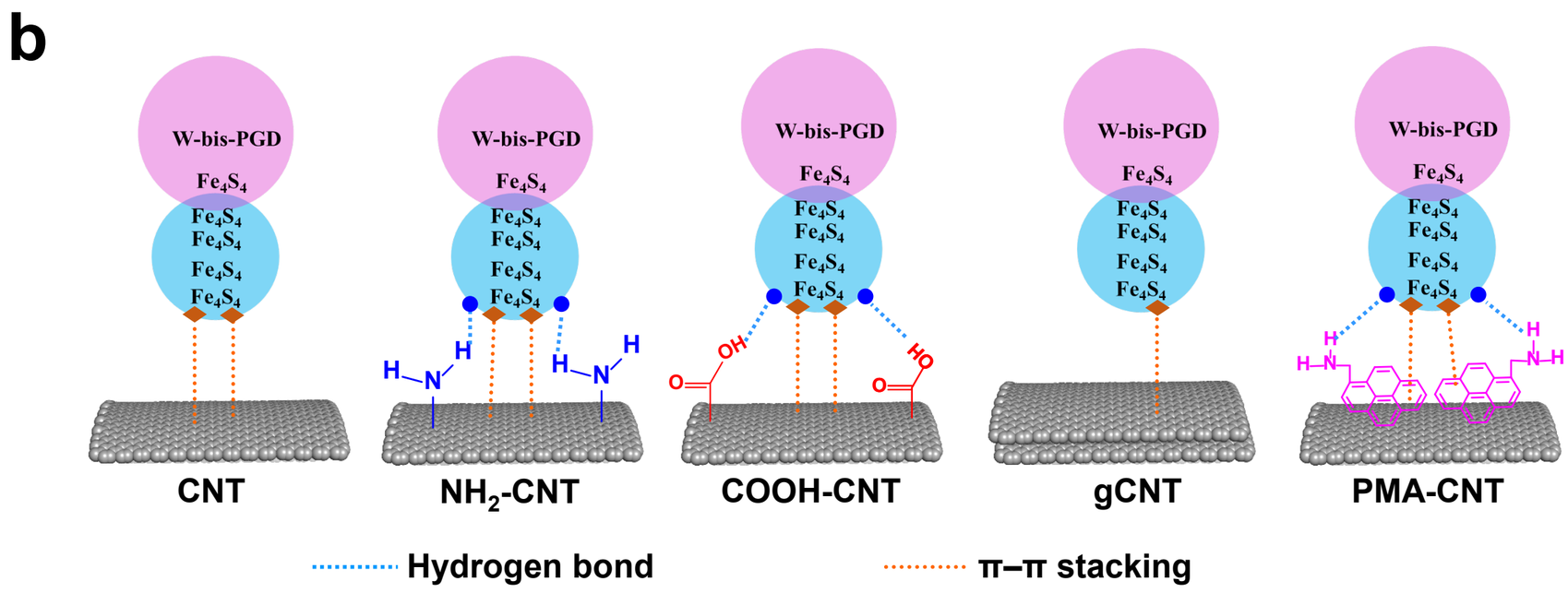
b
W-bis-PGD
Fe4S4
CNT
NH2-CNT
COOH-CNT
gCNT
PMA-CNT
Hydrogen bond
π–π stacking

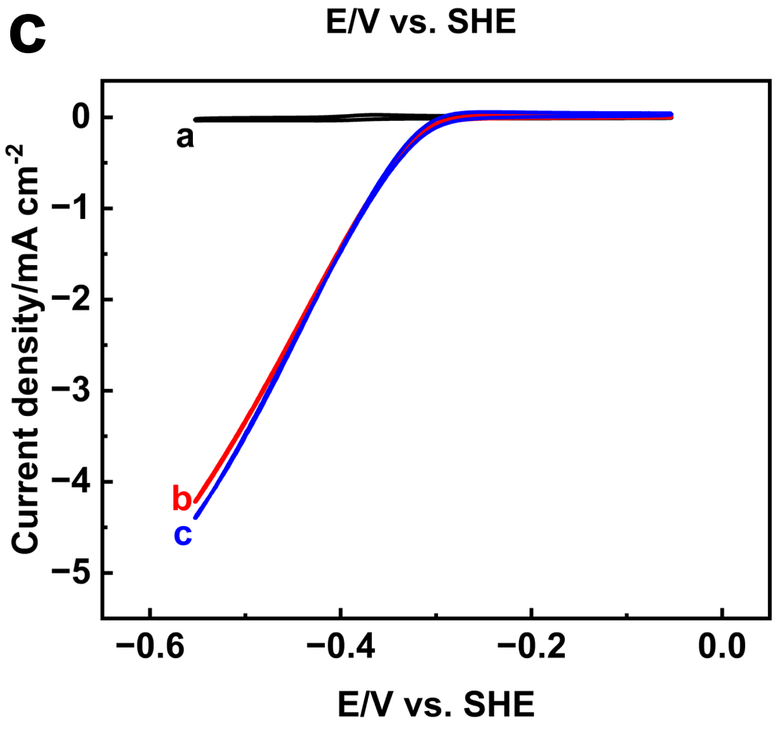
c
E/V vs. SHE
Current density/mA cm-2
a
b
c
0
−1
−2
−3
−4
−5
−0.6
−0.4
−0.2
0.0
E/V vs. SHE

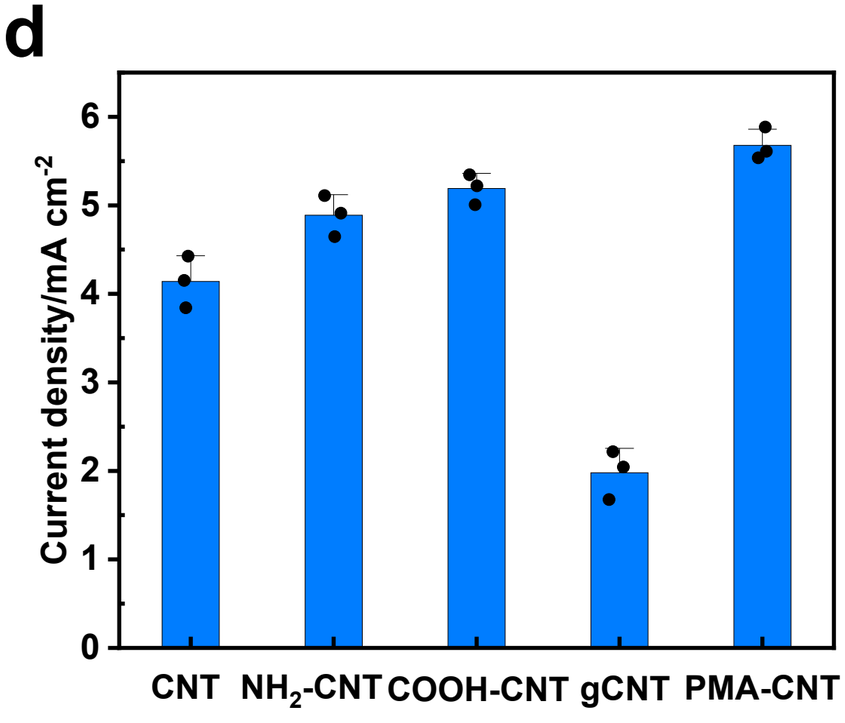
d
Current density/mA cm-2
0
1
2
3
4
5
6
CNT
NH2-CNT
COOH-CNT
gCNT
PMA-CNT

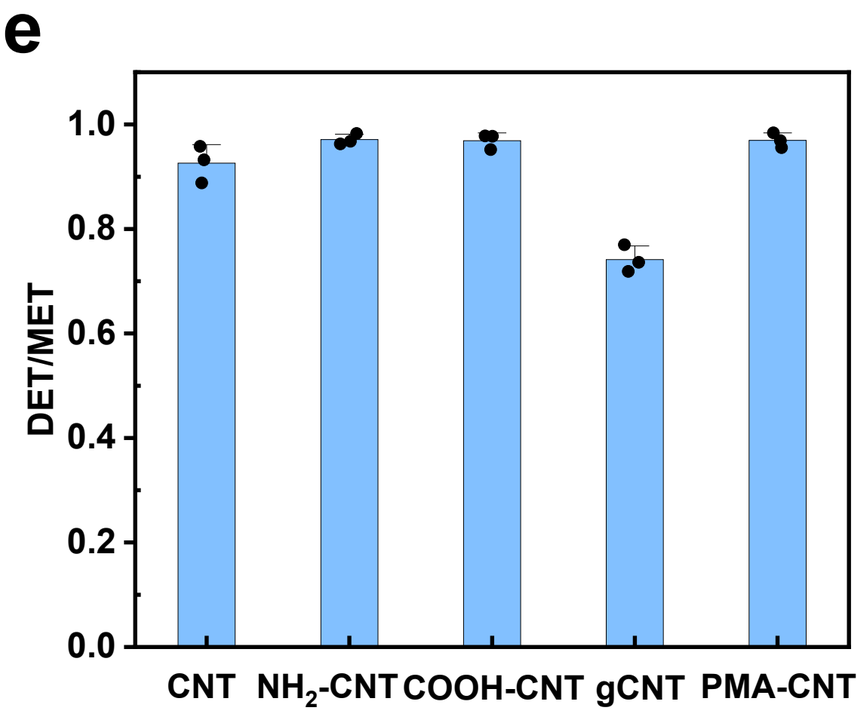
e
DET/MET
0.0
0.2
0.4
0.6
0.8
1.0
CNT
NH2-CNT
COOH-CNT
gCNT
PMA-CNT

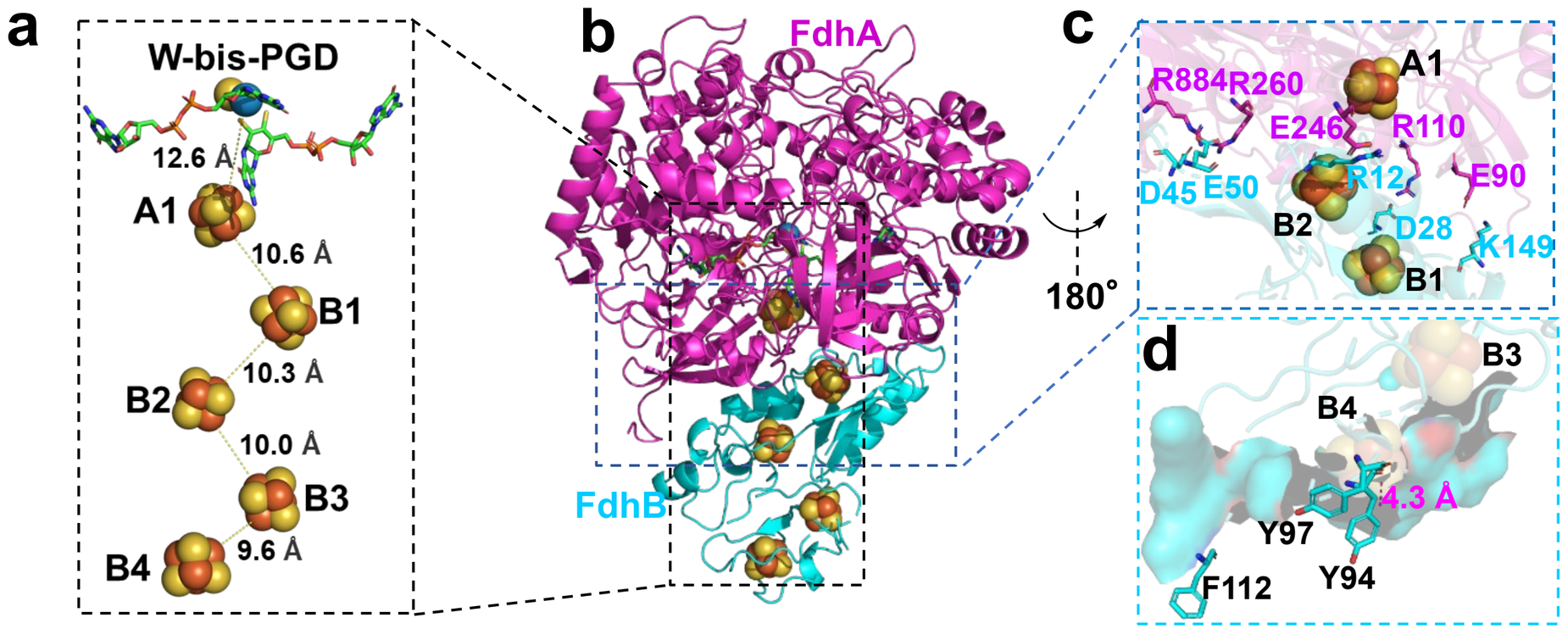
a
W-bis-PGD
12.6 Å
A1
10.6 Å
B1
10.3 Å
B2
10.0 Å
B3
9.6 Å
B4
b
FdhA
FdhB
c
180°
R884
R260
A1
E246
R110
D45
E50
R12
E90
B2
D28
K149
B1
d
B3
B4
4.3 Å
Y97
Y94
F112
e
Relative activity/%
WT
Y97A
Y97F
Y94F
Y94S
f
CNT
NH2-CNT
PMA-CNT
Relative current/%
g
DET/MET
h
17.1 Å
D87
E91
D89
i
E62
I84
G85
T88
V63
K87
3.3 Å
P65

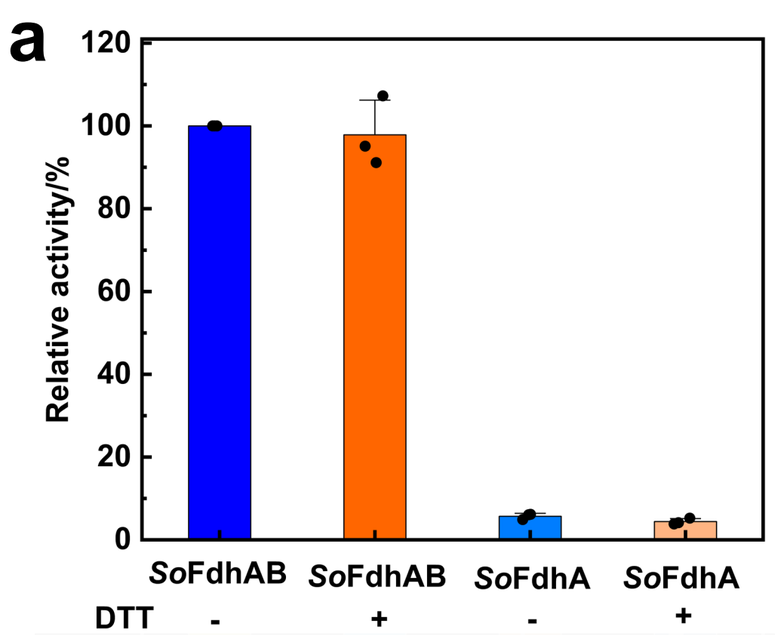
a
Relative activity/%
120
100
80
60
40
20
0
SoFdhAB
SoFdhAB
SoFdhA
SoFdhA
DTT
-
+
-
+

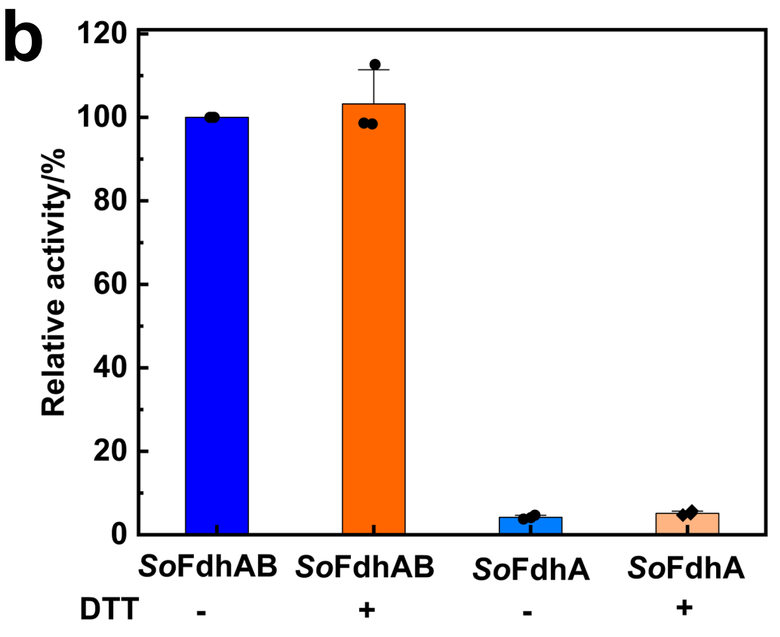
b
Relative activity/%
120
100
80
60
40
20
0
SoFdhAB
SoFdhAB
SoFdhA
SoFdhA
DTT
-
+
-
+

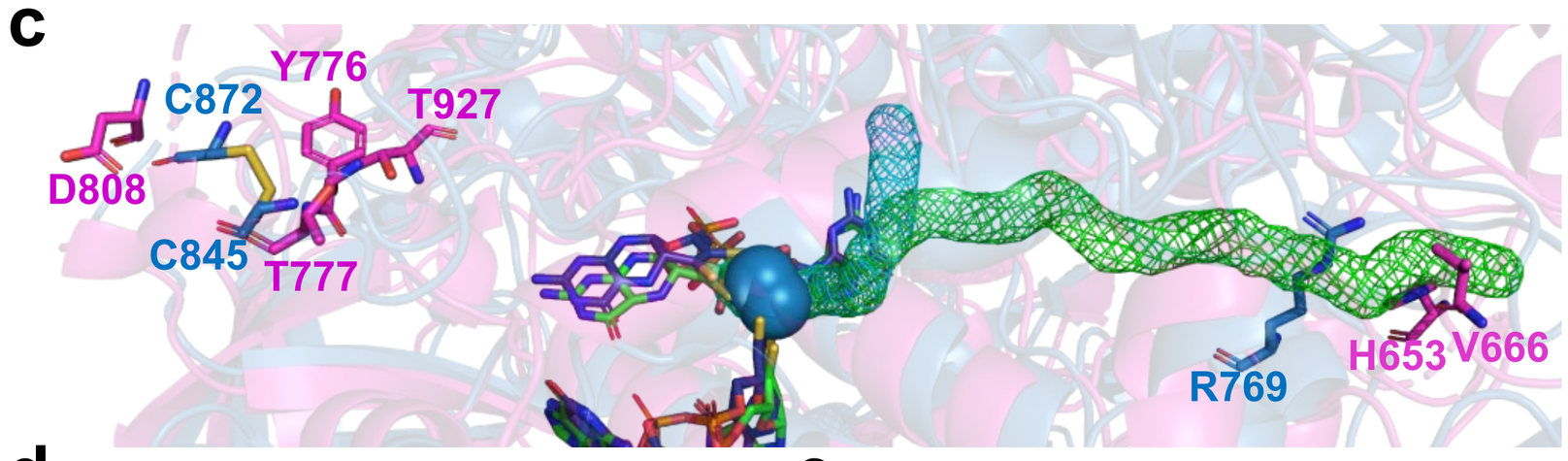
c
Y776
C872
T927
D808
C845
T777
R769
H653
V666

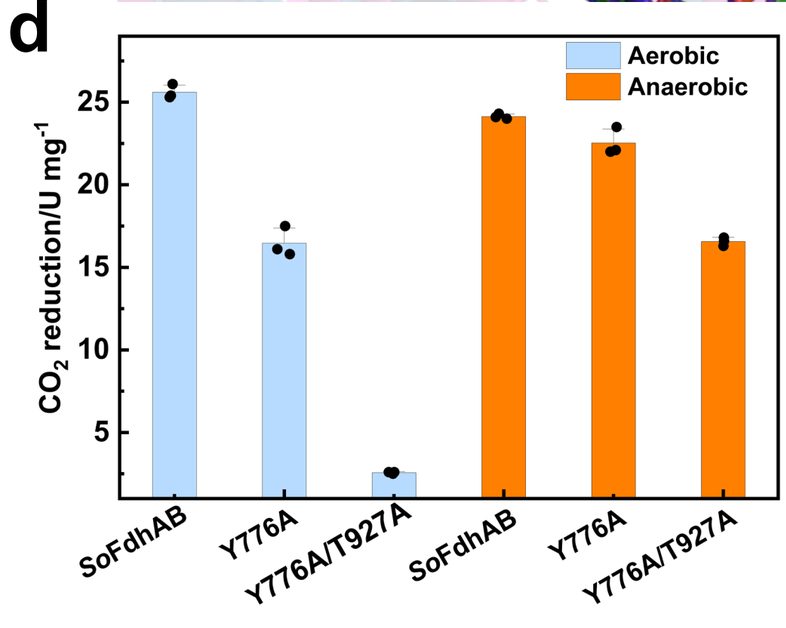
d
Aerobic
Anaerobic
CO2 reduction/U mg-1
25
20
15
10
5
SoFdhAB
Y776A
Y776A/T927A
SoFdhAB
Y776A
Y776A/T927A

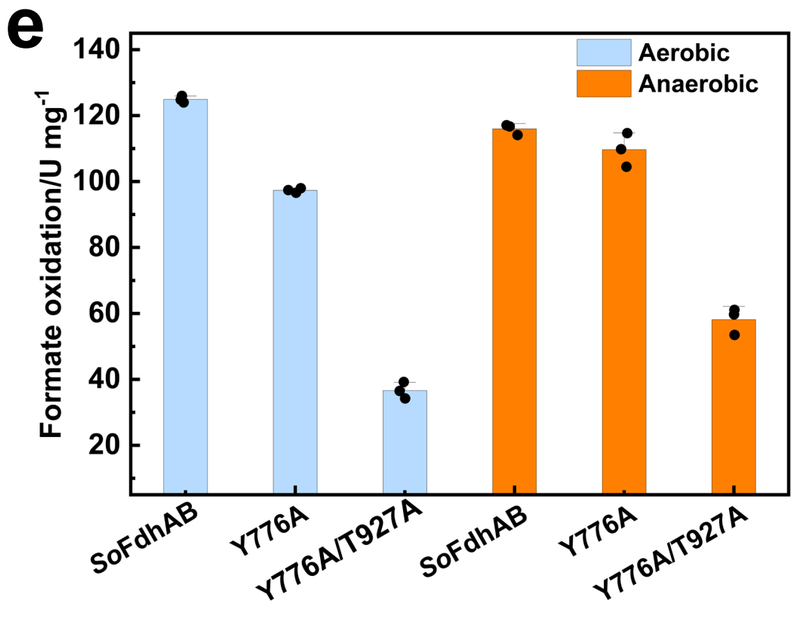
e
Aerobic
Anaerobic
Formate oxidation/U mg-1
140
120
100
80
60
40
20
SoFdhAB
Y776A
Y776A/T927A
SoFdhAB
Y776A
Y776A/T927A

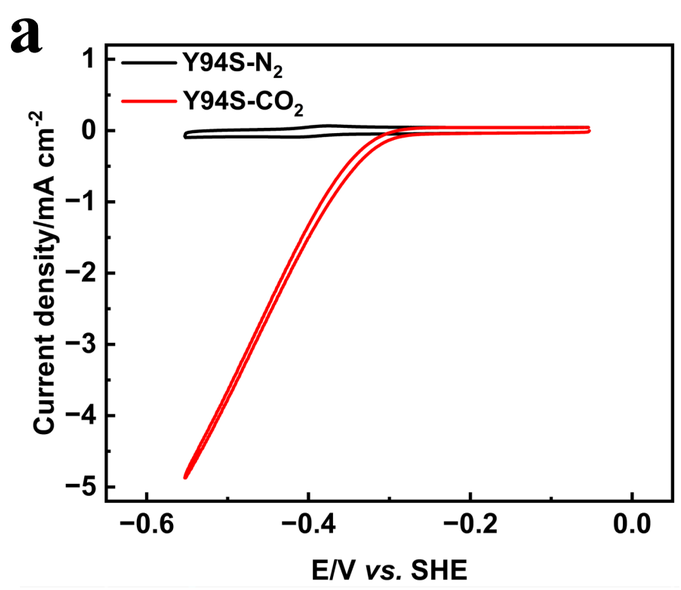
a
Y94S-N2
Y94S-CO2
Current density/mA cm-2
E/V vs. SHE

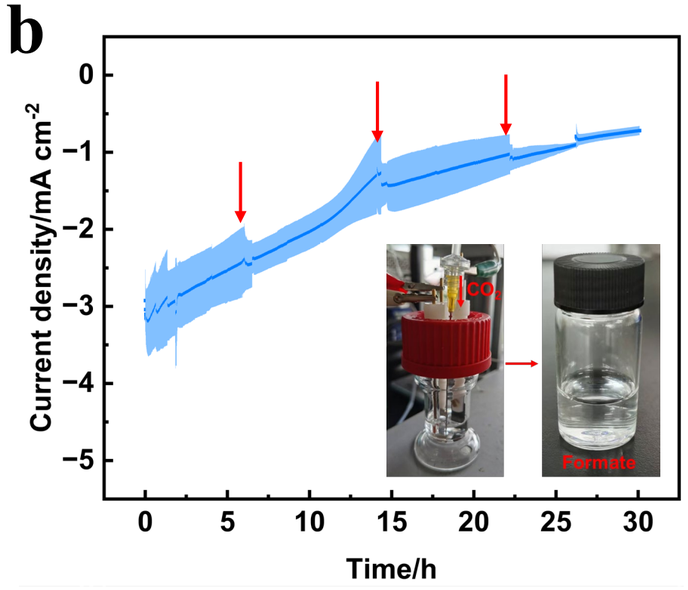
b
Current density/mA cm-2
Time/h
CO2
Formate

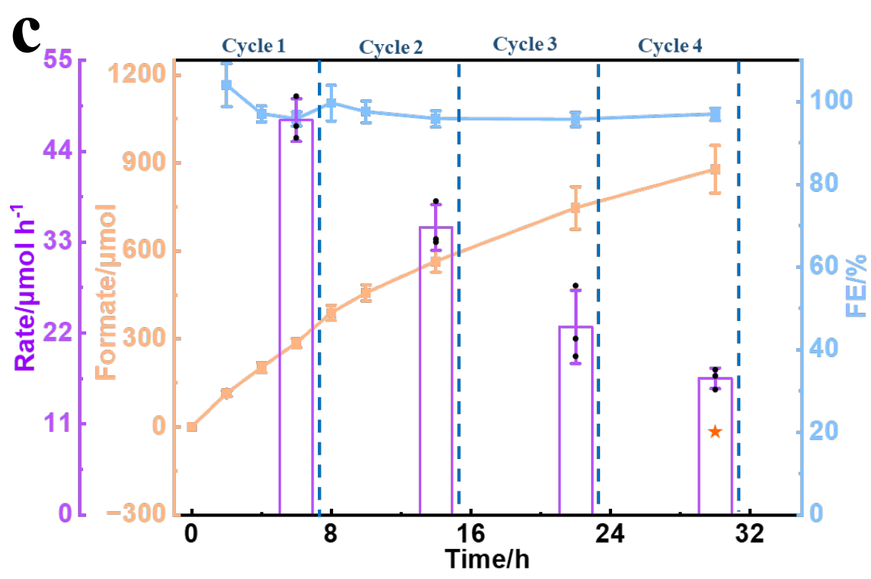
c
Cycle 1
Cycle 2
Cycle 3
Cycle 4
Rate/μmol h-1
Formate/μmol
FE/%
Time/h

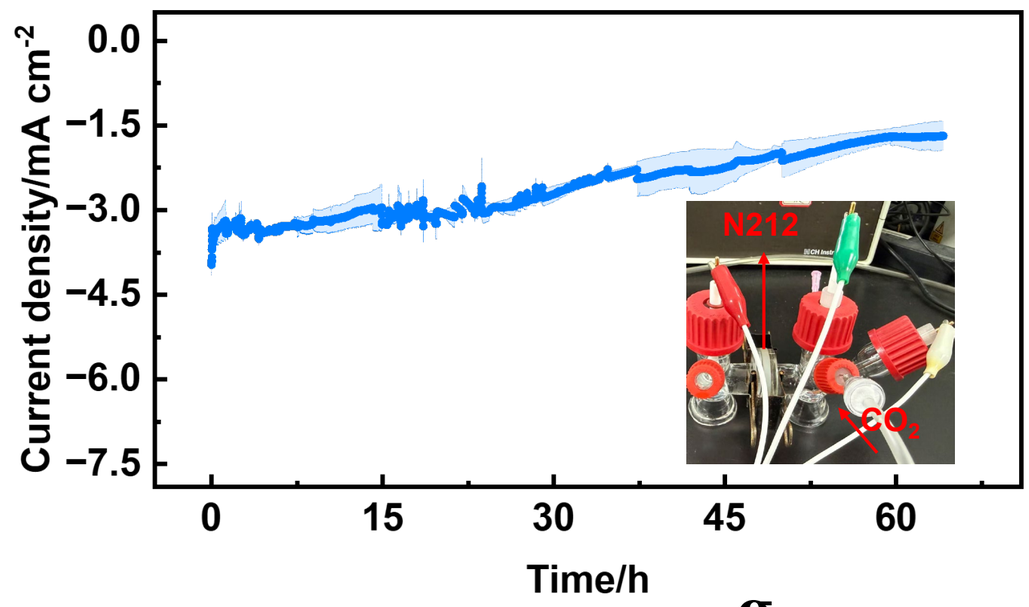
d
Current density/mA cm-2
Time/h
N212
CO2

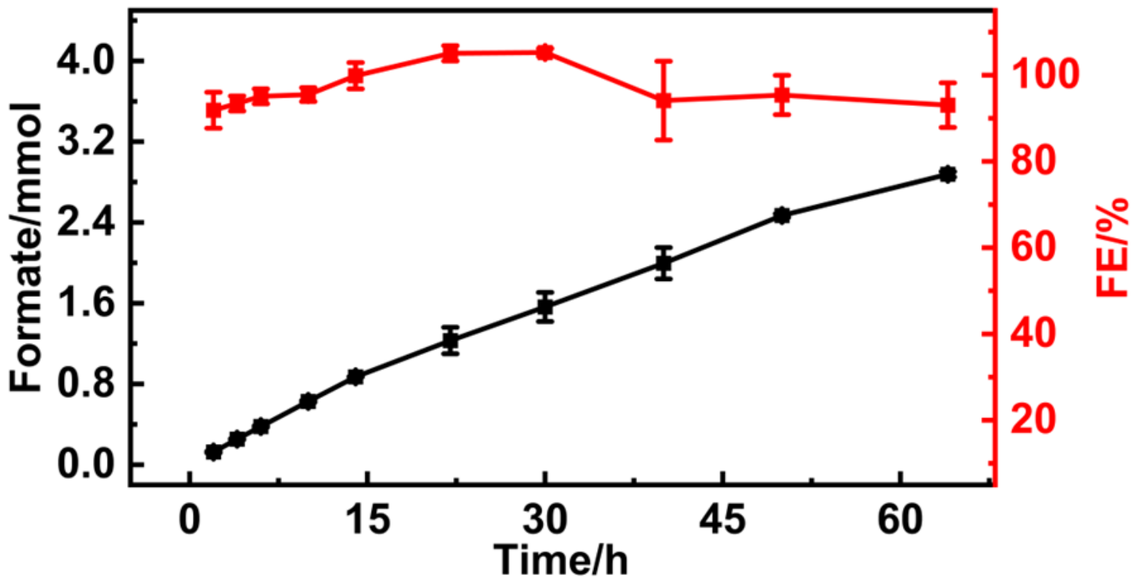
e
Formate/mmol
FE/%
Time/h

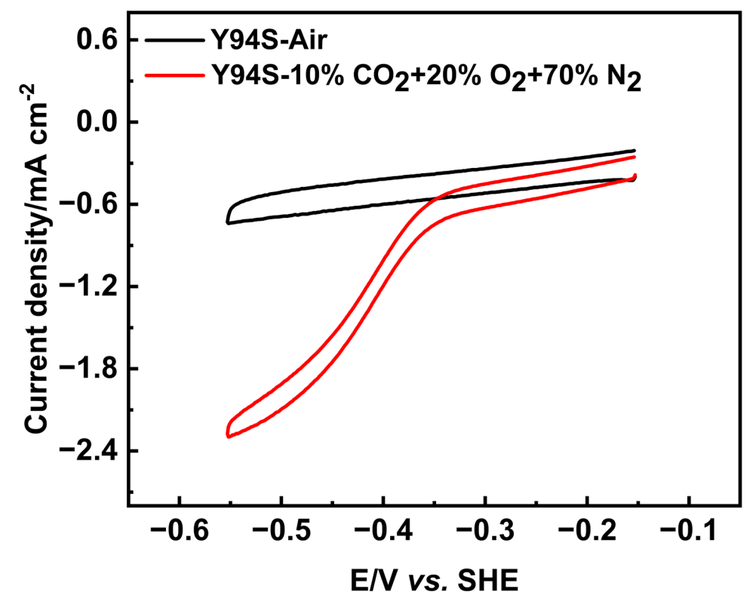
f
Y94S-Air
Y94S-10% CO2+20% O2+70% N2
Current density/mA cm-2
E/V vs. SHE

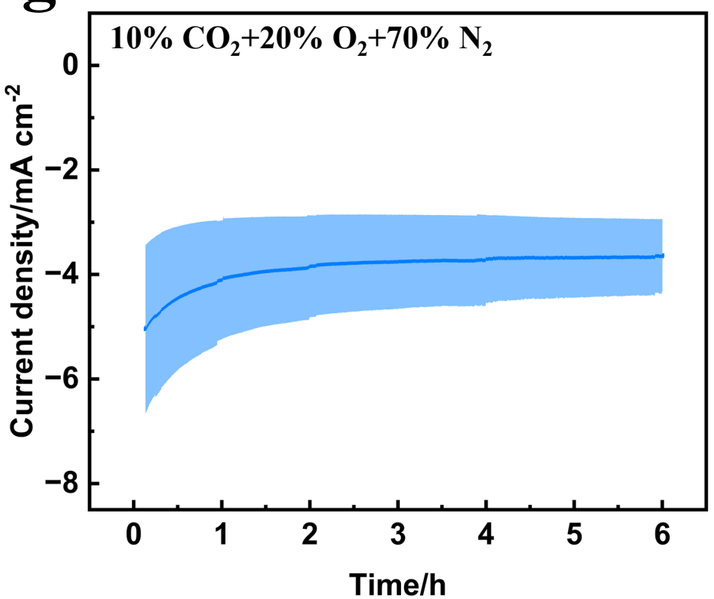
g
10% CO2+20% O2+70% N2
Current density/mA cm-2
Time/h

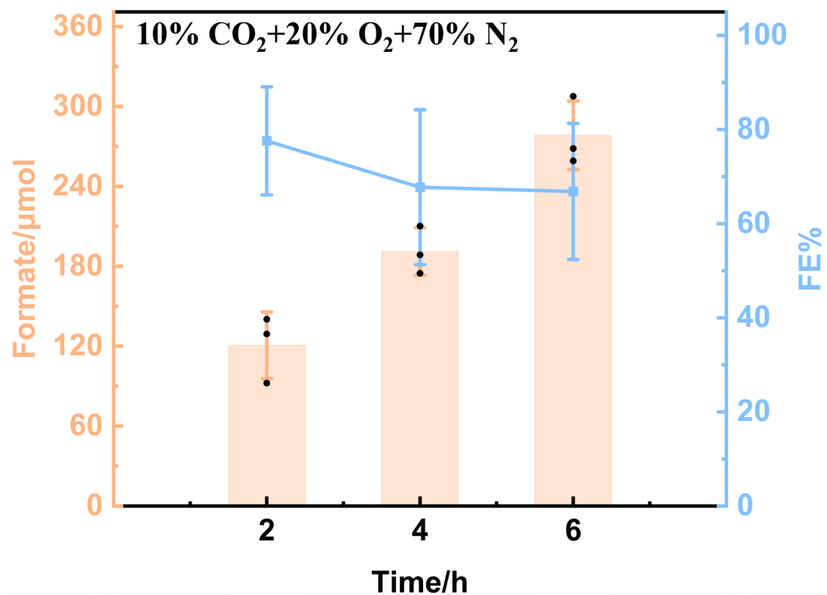
h
10% CO2+20% O2+70% N2
Formate/μmol
FE%
Time/h